

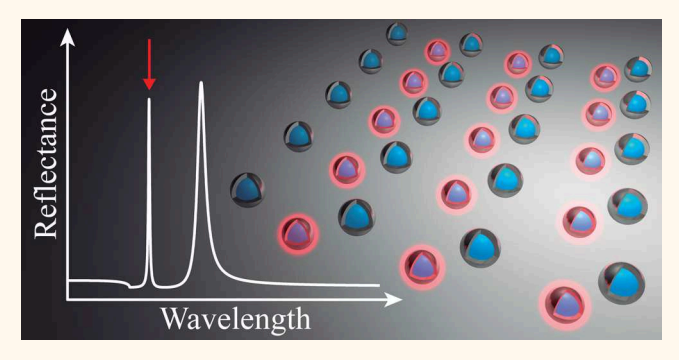
Hybridization of Lattice Resonances

Sebastian Baur, Stephen Sanders, and Alejandro Manjavacas*

Department of Physics and Astronomy, University of New Mexico, Albuquerque, New Mexico 87131, United States

Supporting Information

ABSTRACT: Plasmon hybridization, the electromagnetic analog of molecular orbital theory, provides a simple and intuitive method to describe the plasmonic response of complex nanostructures from the combination of the responses of their individual constituents. Here, we follow this approach to investigate the optical properties of periodic arrays of plasmonic nanoparticles with multiparticle unit cells. These systems support strong collective lattice resonances, arising from the coherent multiple scattering enabled by the lattice periodicity. Due to the extended nature of these modes, the interaction between them is very different from that among localized surface



plasmons supported by individual nanoparticles. This leads to a much richer hybridization scenario, which we exploit here to design periodic arrays with engineered properties. These include arrays with two-particle unit cells, in which the interaction between the individual lattice resonances can be canceled or maximized by controlling the relative position of the particles within the unit cell, as well as arrays whose response can be made either invariant to the polarization of the incident light or strongly dependent on it. Moreover, we explore systems with three- and four-particle unit cells and show that they can be designed to support lattice resonances with complex hybridization patterns in which different groups of particles in the unit cell can be selectively excited. The results of this work serve to advance our understanding of periodic arrays of nanostructures and provide a methodology to design periodic structures with engineered properties for applications in nanophotonics.

KEYWORDS: hybridization, nanoparticle arrays, lattice resonances, plasmons, plasmonic crystals, multiparticle unit cells

etallic nanostructures are well-known to support surface plasmons, which arise from the coupling of collective oscillations of their conduction electrons to external electromagnetic fields. The large near-field and strong interaction cross sections provided by surface plasmons make them exceptional tools to manipulate light at the nanoscale, which has enabled the development of a variety of applications in areas as diverse as solar energy harvesting,^{2,3} photocatalysis, ^{4,5} ultrasensitive biosensing, ^{6,7} and nanoscale light emission. ⁸⁻¹⁰

When two or more metallic nanostructures are placed together, the near-fields generated by the surface plasmons supported by each of them result in strong interactions that completely modify the optical response of the whole system. 1 The properties of the resulting collective plasmonic resonances are entirely determined by the spatial distribution of the individual nanostructures, in much the same way that the orbitals of a molecule are governed by the geometrical arrangement of the atomic orbitals of its constituents. 12 This analogy is the basis of the plasmon hybridization model, 13 which allows one to describe, in a simple and intuitive manner, the plasmonic response of ensembles of nanostructures from the combination of the plasmons of their individual components. For example, as sketched in Figure 1a, when

two identical nanoparticles are placed in close proximity, their dipolar plasmons interact, resulting in two new hybrid resonances, commonly referred to as bonding and antibonding modes, 14,15 with energies dictated by the characteristics of the interaction. Plasmon hybridization has been used extensively to describe the plasmonic response of a variety of metallic nanostructures such as nanoshells, 16-18 nanocrescents, 19,20 and nanocavities,^{21–23} as well as graphene nanostructures with different geometries.^{24–27} Moreover, this approach has been used to understand the Fano resonances 28-30 supported by plasmonic metamolecules, ^{31–34} to interpret electron energy loss experiments, 35-38 and to design building blocks for metamaterials 39,40 and nanostructures with nonlinear 41,42 or chiral responses.43,44

Although these examples involve finite ensembles of nanostructures, plasmon hybridization is expected to describe, as well, the interaction between extended systems, such as periodic arrays of nanoparticles. These systems are well-known to support lattice resonances arising from the coherent multiple scattering enabled by the periodicity of the structure, 45

Received: November 18, 2017 Accepted: January 4, 2018 Published: January 4, 2018

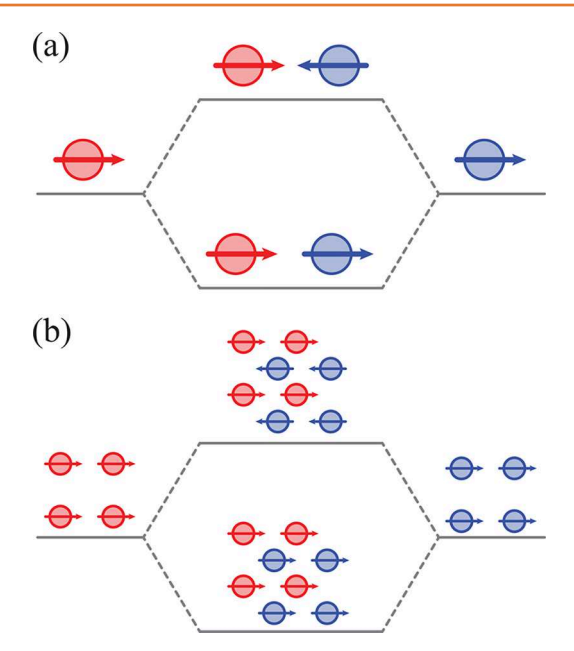


Figure 1. Summary of plasmon hybridization model. (a) Hybridization diagram for two identical plasmonic nanoparticles. When considered individually, each nanoparticle supports a dipolar mode. However, if the particles are placed together, the interaction between the dipolar modes leads to the formation of two hybridized modes, commonly referred to as bonding and antibonding, with energies determined by the strength of the interaction. (b) Hybridization diagram for two periodic arrays of plasmonic nanoparticles. Similar to the case of individual particles, the interaction between the lattice resonances of two identical arrays leads to the formation of hybridized lattice resonances when the arrays are placed in the same plane.

which appear at wavelengths commensurate with the lattice periodicity and display very narrow line shapes, ⁴⁹ thus leading to very strong optical responses. ^{50–53} For that reason, periodic

arrays of nanostructures have been used to design light-emitting devices, ^{8,54-64} sensors, ^{7,65,66} perfect absorbers, ⁶⁷⁻⁶⁹ and platforms for quantum information processing, ⁷⁰⁻⁷⁴ as well as to investigate other interesting physical phenomena. ^{75,76} However, the majority of nanoparticle arrays considered in the past are built using single-particle unit cells, that is, associated with one of the five two-dimensional Bravais lattices, ⁷⁷ which imposes a limitation to the complexity of the near- and far-field responses of these systems. On the contrary, arrays built from the repetition of unit cells containing more than one particle, that is, using non-Bravais lattices, present more involved responses ⁷⁸⁻⁸³ and, consequently, offer a broader range of possibilities to engineer their optical properties. ^{84,85}

In this article, we employ a plasmon hybridization approach to investigate the response of periodic arrays of nanoparticles with multiparticle unit cells. These systems can be seen as the superposition of several identical arrays (one per particle in the unit cell), which are displaced with respect to each other along the plane in which they lie. The response of the whole array is then determined by the interaction of the lattice resonances supported by the individual constituents, as sketched in Figure 1b, in the same way as the bonding and antibonding modes of a dimer arise from the hybridization of the dipolar plasmons of the particles that form it. However, due to the extended nature of the lattice resonances, the interaction between them, which occurs mainly through far-field coupling, is very different from that among localized surface plasmons, which is governed by near-field coupling. In particular, we show that, by controlling the relative position of the particles within the unit cell, it is possible to manipulate, and even cancel, the interaction between the corresponding lattice resonances. This results in a much richer hybridization scenario, which we exploit to design arrays with engineered properties. Our study furthers the knowledge of the response of periodic arrays of nanoparticles and provides tools for designing nanophotonic platforms.

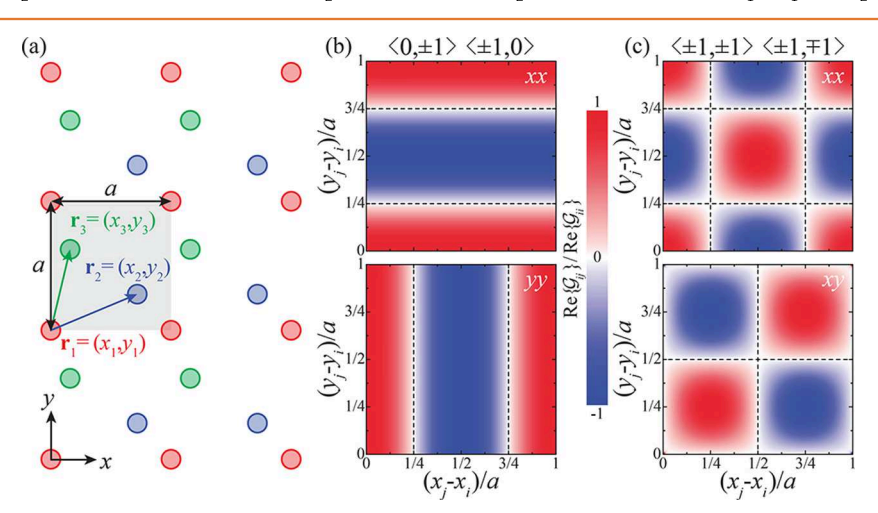


Figure 2. Periodic arrays of plasmonic nanoparticles with multiparticle unit cells. (a) Sketch of the system under study, built from the periodic repetition of a unit cell containing N particles (shaded area) over a square lattice with periodicity a. The different particles in the unit cell are placed at distances $r_i = (x_{ij}y_i)$, with i = 1,...,N from the lattice nodes. For simplicity, we always choose to place particle 1 at the lattice nodes (i.e., $x_1 = 0$, $y_1 = 0$). (b,c) Real part of the lattice sum \mathcal{G}_{ij} normalized to the real part of \mathcal{G}_{ij} , calculated as a function of the relative position between particles j and i for normal incidence. (b) Results calculated at the $\langle 0,\pm 1 \rangle$, $\langle \pm 1,0 \rangle$ Rayleigh anomaly, which, for a square lattice, occurs at $\lambda = a$. The upper (lower) plot corresponds to the xx (yy) component of the lattice sum. (c) Results for the $\langle \pm 1,\pm 1 \rangle$, $\langle \pm 1,\mp 1 \rangle$ Rayleigh anomaly, which appears in the spectrum at $\lambda = a/\sqrt{2}$. The upper plot corresponds to the xx component, which, in this case, is identical to the yy one, whereas the lower one corresponds to the xy component.

RESULTS

The system under study is depicted in Figure 2a. It consists of a periodic array built from the repetition of a unit cell containing N nanoparticles (shaded area) over a square lattice of period a. The array lies in the xy-plane, and the positions of the different particles in the unit cell, measured from the lattice nodes, are \mathbf{r}_i = (x_i, y_i) , with i = 1, 2, ..., N. For simplicity, we assume that particle 1 is always located at the lattice node (i.e., $x_1 = 0$, $y_1 =$ 0). The optical response of this system can be described using the well-established coupled dipole model. 45,46,52,60,86 Within this approach, which is valid for particles with small dimensions compared with both the wavelength and the interparticle distance, each of the particles is modeled as a point dipole $\mathbf{p}_{i,u}$ with a certain polarizability α_i . We use greek indices to denote the unit cell to which the particle belongs and latin ones to label the different particles within a unit cell. Upon illumination by an external field $\mathbf{E}_{i,u}$ the dipoles induced in the particles satisfy

$$\mathbf{p}_{i,\mu} = \boldsymbol{\alpha}_i \mathbf{E}_{i,\mu} + \boldsymbol{\alpha}_i \sum_{\nu}^{\prime} \sum_{j=1}^{N} \mathbf{G}_{ij,\mu\nu} \mathbf{p}_{j,\nu}$$
(1)

where $G_{ii,\mu\nu}$ is the dipole-dipole interaction tensor, defined as

$$\mathbf{G}_{ij,\mu\nu} = \left[k^2 + \nabla\nabla\right] \frac{\mathrm{e}^{ik|\mathbf{T}_{\mu} + \mathbf{r}_i - \mathbf{T}_{\nu} - \mathbf{r}_j|}}{|\mathbf{T}_{\mu} + \mathbf{r}_i - \mathbf{T}_{\nu} - \mathbf{r}_j|}$$

Here, $T_{\mu} - T_{\nu}$ is the distance between the μ and ν unit cells, $k = 2\pi/\lambda$ is the wave vector, and λ is the light wavelength. The prime in the first summation indicates that the terms $\nu = \mu$ are excluded from it when i = j because a dipole does not interact with itself. Due to the periodicity of the array, the solutions of eq. 1 satisfy Bloch's theorem and can be written as $\mathbf{p}_{i,\mu} = \mathbf{p}_i(\mathbf{k}_{\parallel})$ $e^{i\mathbf{k}_{\parallel} \cdot T_{\mu}}$. Using this expression, we can solve eq. 1 to obtain

$$\mathbf{p}_{i}(\mathbf{k}_{\parallel}) = \sum_{j=1}^{N} \mathbf{M}_{ij}^{-1}(\mathbf{k}_{\parallel}) \mathbf{E}_{j}(\mathbf{k}_{\parallel})$$
(2)

where $\mathbf{M}(\mathbf{k}_{\parallel}) = \boldsymbol{\alpha}^{-1} - \mathcal{G}(\mathbf{k}_{\parallel})$ is a $3N \times 3N$ matrix, and $\mathcal{G}_{ij}(\mathbf{k}_{\parallel}) = \Sigma_{\nu}' \mathbf{G}_{ij,\nu 0} \mathrm{e}^{-i\mathbf{k}_{\parallel}' \mathbf{T}_{\nu}}$ is the Fourier transform of the dipole—dipole interaction tensor, commonly known as the lattice sum. This quantity contains all of the information on the geometry of the array and therefore determines its optical response. In particular, it controls the existence and properties of the lattice resonances supported by the periodic array, which appear at wavelengths where the real part of the determinant of \mathbf{M} vanishes. Such behavior happens in the vicinity of the Rayleigh anomalies, where $\mathcal{G}_{ij}(\mathbf{k}_{\parallel})$ diverges. These spectral features are located at wavelengths satisfying $\lambda_{\mathbf{q}} = 2\pi/|\mathbf{k}_{\parallel} + \mathbf{q}|$, with \mathbf{q} representing the reciprocal lattice vectors, as explained in the Methods section.

A periodic array with a multiparticle unit cell can be seen as the superposition of N identical single-particle arrays, all with the same periodicity, which are displaced with respect to each other along the xy-plane. From this perspective, the diagonal terms of $\mathcal{G}_{ij}(\mathbf{k}_{\parallel})$, which are all equal, determine the position of the lattice resonances for the isolated single-particle array. On the other hand, the off-diagonal terms of $\mathcal{G}_{ij}(\mathbf{k}_{\parallel})$ represent the interaction between the single-particle arrays corresponding to particles i and j and therefore are symmetric under $i \leftrightarrow j$. Then, by analyzing $\mathcal{G}_{ij}(\mathbf{k}_{\parallel})$, we can understand and predict the lattice resonances of the multiparticle unit cell array, which arise from

the hybridization of the lattice resonances supported by each of the individual single-particle arrays, in the same way that the hybridized plasmons supported by a particle dimer can be understood from the analysis of the interaction between the plasmons of its individual constituents (see Figure 1). However, in contrast to the interaction between localized plasmons, which is governed by the near-field coupling and hence always has the same sign, $G_{ii}(\mathbf{k}_{||})$ is dominated by the far-field coupling (see Methods section) and therefore displays a much more complex behavior, as shown in Figure 2b,c. There, we plot the real part of the lattice sum as a function of the relative position of particle *j* measured with respect to particle *i*. Here and in the following, we assume normal incidence (i.e., $\mathbf{k}_{\parallel} = 0$). The values of Re $\{G_{ii}\}$ are normalized to those of the corresponding diagonal term Re $\{G_{ii}\}$. Panel (b) shows the results calculated near the $(0,\pm 1)$, $(\pm 1,0)$ Rayleigh anomaly, which, for a square lattice, is degenerate and appears in the spectrum at $\lambda = a$. Notice that we use the notation $\langle m,n \rangle$ to label the Rayleigh anomaly corresponding to the reciprocal lattice vector $\mathbf{q} = \frac{2\pi}{a}(m, n)$ (see Methods). The upper and lower plots correspond, respectively, to the xx and the yy components of the lattice sum. Panel (c), on the other hand, displays the results for the $\langle \pm 1,\pm 1 \rangle$, $\langle \pm 1,\mp 1 \rangle$ Rayleigh anomaly, which is also degenerate for a square lattice, appearing at $\lambda = a/\sqrt{2}$. In this case, the upper plot corresponds to the xx component, which is equal to the yy one, whereas the lower one corresponds to the xy component. All of these plots are calculated at wavelengths that are infinitesimally larger than those of the corresponding Rayleigh anomalies, for which the real part of the lattice sum dominates and a lattice resonance exists, 52,86 as explained in the Methods section (see also Figure S1 in the Supporting Information). These results are expected to change as the wavelength departs from the Rayleigh anomaly, although, as shown in Figures S2 and S3, the main features are significantly robust.

Examining Figure 2b,c, we clearly see that the different components of Re $\{G_{ii}\}$ take values ranging approximately from $-\text{Re}\{\mathcal{G}_{ii}\}\$ (blue region) to $\text{Re}\{\mathcal{G}_{ii}\}\$ (red region) depending on the relative position of particle j with respect to particle i. As a consequence of this, the lattice sums vanish for some relative positions, which are indicated by the dashed lines in the figure. Expectedly, the number and the geometrical arrangement of these lines are dictated by the reciprocal lattice vector associated with the corresponding Rayleigh anomaly, as explained in the Methods section. We provide more examples of the lattice sums corresponding to higher-order Rayleigh anomalies in the Supporting Information (see Figures S4 and S5). Furthermore, although in this work we assume normal incidence, $k_{\parallel} = 0$, the analysis presented here can be generalized to $\mathbf{k}_{\parallel} \neq 0$. In such a case, the degeneracy of the Rayleigh anomalies is lifted, leading to a more complicated set of outcomes (see Methods).

The behavior of \mathcal{G}_{ij} shown in Figure 2 enables a richer hybridization scenario compared to that of localized surface plasmons. This can be exploited to engineer the optical response of multiparticle unit cell arrays through the control of the interaction between their single-particle constituents. As discussed before, the lattice resonances of a periodic array with a multiparticle unit cell are governed by \mathcal{G}_{ij} . More specifically,

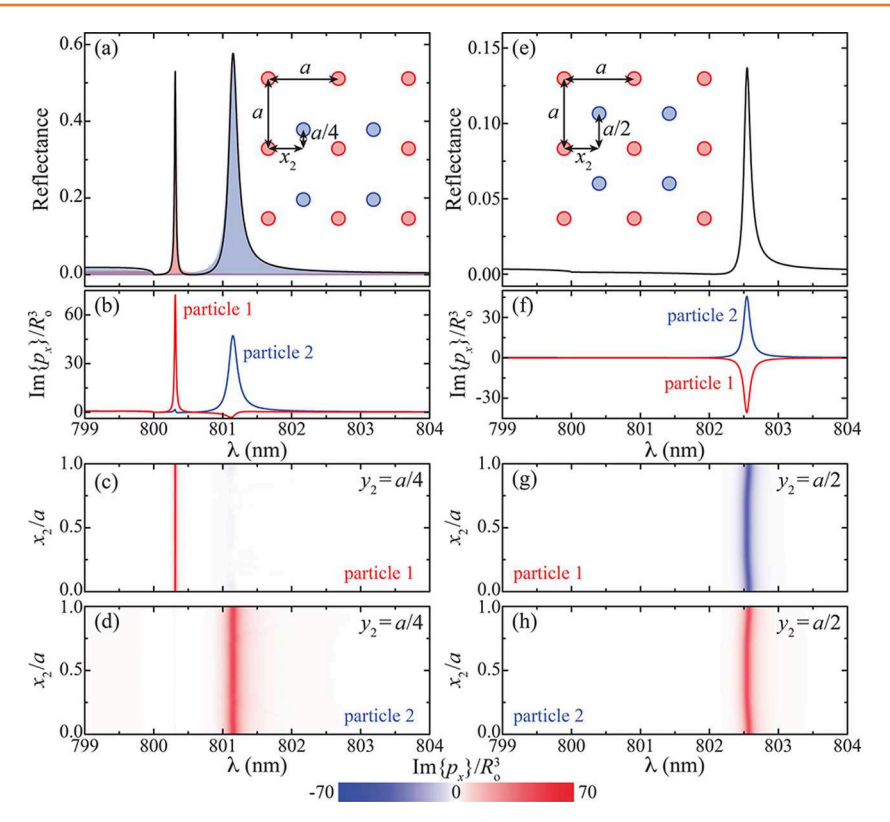


Figure 3. Hybridization of lattice resonances. (a) Black curve shows the reflectance for an array composed of a square lattice with periodicity a = 800 nm and a two-particle unit cell (see inset), in which particle 1 (red) is located at the lattice nodes (i.e., $x_1 = 0$, $y_1 = 0$) and particle 2 (blue) is placed at $x_2 = a/2$, $y_2 = a/4$. Both particles are silver nanoshells with silica cores. The inner and outer radii are $R_i = 40$ nm, $R_0 = 50$ nm for particle 1 and $R_i = 50$ nm, $R_0 = 60$ nm for particle 2. The red and blue shadowed areas represent the reflectance of the red and blue arrays when considered individually. (b) Imaginary part of the dipole induced in particle 1 (red curve) and particle 2 (blue curve) for the lattice considered in panel (a). (c,d) Imaginary part of the dipole induced in particle 1 (c) and particle 2 (d) of the lattice of panel (a) as a function of x_2 . (e-h) Same as (a-d) but for the case in which particle 2 is placed at $x_2 = a/2$, $y_2 = a/2$ (see inset). In all cases, the incident light is polarized along the x-axis, and the polarizability is normalized to R_0^3 .

they correspond to the solution of the following eigenvalue problem

$$\sum_{j} \boldsymbol{\alpha}_{i} \mathcal{G}_{ij} \mathbf{p}_{j} = \mathbf{p}_{i} \tag{3}$$

which is derived from eq 2 in absence of external field.

As a first example of an application of these ideas, let us consider a square array with periodicity a and a two-particle unit cell, operating on the red side of the $\langle 0,\pm 1 \rangle$, $\langle \pm 1,0 \rangle$ Rayleigh anomaly (i.e., near $\lambda=a$). Assuming nanoparticles with spherical symmetry, at normal incidence the induced dipoles must lie in the plane of the array (i.e., the xy-plane). This, together with the vanishing of the xy component of the lattice sum for the considered Rayleigh anomaly, as shown in Figure S2, allows us to consider the xx and the yy components separately. Therefore, without loss of generality, we can focus on the xx component, which is the only relevant one for illumination with x-polarized light (identical results are obtained for the yy component under y-polarized illumination). Under these conditions, the lattice sum reduces to the following 2×2 matrix

$$\mathcal{G} = \begin{pmatrix} \mathcal{G}_{11} & \mathcal{G}_{12} \\ \mathcal{G}_{12} & \mathcal{G}_{11} \end{pmatrix}$$

The diagonal term \mathcal{G}_{11} is independent of the relative position between particles 1 and 2; however, \mathcal{G}_{12} depends on it, as

shown in the upper panel of Figure 2b. In particular, when particle 1 is located at the lattice nodes (i.e., $x_1 = 0$, $y_1 = 0$) and particle 2 is at $x_2 = a/2$, $y_2 = a/4$, the real part of \mathcal{G}_{12} vanishes, and hence, G becomes diagonal because its real part dominates on the red side of the Rayleigh anomaly, as shown in Figure S1. Then, by solving eq 3, we find that the array supports two different lattice resonances, which appear in the spectrum at wavelengths λ_1 and λ_2 , satisfying $\operatorname{Re}\{\alpha_1^{-1}\}=\operatorname{Re}\{\mathcal{G}_{11}\}$ and $\operatorname{Re}\{\alpha_2^{-1}\}=\operatorname{Re}\{\mathcal{G}_{11}\}$, respectively. Using the notation $\mathbf{p}=$ (p_{1x},p_{2x}) , the associated dipole mode for the first resonance is (1,0), whereas for the second one, it is (0,1). This means that the two single-particle arrays, in which the two-particle system can be divided, do not interact. Therefore, if particles 1 and 2 have different polarizabilities, the multiparticle array supports two different resonances, each of them involving only the excitation of one of the two particles.

This prediction is verified in Figure 3a for a two-particle array of silver nanoshells with silica cores and periodicity a=800 nm. Particle 1 (red) has an inner radius of $R_{\rm i}=40$ nm and an outer radius of $R_{\rm o}=50$ nm, whereas for particle 2 (blue), $R_{\rm i}=50$ nm and $R_{\rm o}=60$ nm. The black curve shows the reflectance of this array calculated numerically, using the coupled dipole model previously described. The polarizability of the nanoshells is obtained from the dipolar Mie scattering coefficient and therefore includes retardation effects (see Methods). The coupled dipole model is expected to be accurate for particles with subwavelength dimensions, for which the contribution of

higher-order modes is small, separated by distances of at least three radii. In order to verify the validity of this model, we have benchmarked it against full-wave results obtained through a finite element method (FEM) simulation (see Figures S6 and S7 in the Supporting Information). As anticipated, the multiparticle array supports two lattice resonances on the red side of the Rayleigh anomaly located at 800 nm. These two peaks are almost identical to the reflectance peaks that each of the two single-particle arrays, in which the multiparticle array can be divided, support when considered individually, which are depicted by the red and blue shaded areas. This confirms the noninteracting nature of these lattice resonances.

We can gain more insight into the response of this array by analyzing the dipole induced in each of the particles. This is done in panel (b), where we plot the imaginary part of the xcomponent of the dipole induced in particle 1 (red curve) and particle 2 (blue curve), normalized to R_0^3 . We choose to analyze the imaginary part because, at resonance, it dominates over the real part and, as opposed to the absolute value, it retains the information about the phase. Examining these results, we observe that, for the first lattice resonance, particle 1 is strongly excited, whereas particle 2 displays almost no induced dipole. This behavior is completely reversed for the second lattice resonance, thus confirming that, for the particular arrangement under investigation, the two single-particle arrays do not interact and therefore behave as if they were isolated. This behavior is further supported by the induced charge and field enhancement calculated with the FEM approach, which are shown in Figure S6. Interestingly, the same outcome is expected for any value of x_2 , provided $y_2 = a/4$, because, as shown Figure 2b, the real part of \mathcal{G}_{12} vanishes along the line y_2 = a/4. This is confirmed by Figure 3c,d, where we plot the imaginary part of the x component of the dipole induced in particle 1 (c) and particle 2 (d) as a function of x_2 .

The behavior of the two-particle array changes dramatically if particle 2 is moved to $x_2 = a/2$, $y_2 = a/2$. In this case, $Re\{G_{12}\} = -Re\{G_{11}\}$, and we therefore expect maximum interaction between particles 1 and 2. Solving eq 3, we find that, in this case, the system supports only one lattice resonance, located at the wavelength satisfying the condition $Re\{(\alpha_1 + \alpha_2)^{-1}\} = Re\{\mathcal{G}_{11}\}$, whose associated dipole mode is proportional to $(-\alpha_1,\alpha_2)$. This means that the dipoles induced in particles 1 and 2 oscillate in opposite directions. These predictions are confirmed by the numerical results shown in Figure 3e,f. In the former, we plot the reflectance of an array identical to that of panel (a), but in which particle 2 is placed at position $x_2 = a/2$, $y_2 = a/2$. As expected, the reflectance shows a single peak located at a wavelength larger than that of the array of panel (a). Examining the corresponding induced dipole shown in panel (f), we observe that, at the lattice resonance, the dipole induced in particle 1 (red curve) has the opposite sign to that of particle 2 (blue curve), thus confirming our prediction (see Figure S6 for the associated induced charge and field enhancement calculated with the FEM simulations). An identical behavior is obtained when x_2 is varied, while keeping $y_2 = a/2$, as shown in panels (g,h), where we plot the imaginary part of the x component of the dipole induced in particle 1 (g) and particle 2 (h) as a function of x_2 . This is in accordance with the fact that $Re\{G_{12}\} = -Re\{G_{11}\}$ for all relative positions with $y_2 = a/2$, as shown Figure 2b.

The behavior of this two-particle array can also be intuitively understood by examining the field enhancement maps shown in Figure S6. Specifically, when $x_2 = a/2$ and $y_2 = a/4$, both particles are located exactly at the node of the lattice resonance associated with the other, and therefore do not interact. If, on the other hand, particle 2 is displaced to $x_2 = a/2$, $y_2 = a/2$, then both particles sit in an antinode of the lattice resonance but with opposite phase, and their corresponding induced dipoles therefore point in opposite directions. This intuitive approach also helps one to understand the limitations of the coupled dipole model; when the size of the particle becomes a significant fraction of the wavelength, higher-order modes could be excited despite the cancelation of the dipole mode (see Figure S7). Unfortunately, as the complexity of the array grows, its behavior becomes less intuitive.

It is important to note that, if particle 2 is placed at a position for which the xx and yy components of Re $\{G_{12}\}$ take different values, then the two-particle array will display a different response when illuminated with x- or y-polarized light. This behavior can be exploited to design arrays with complex anisotropic responses and therefore can complement and enhance anisotropic responses induced by the morphology of the particles. To illustrate this possibility, we consider an array composed of a square lattice with periodicity a = 800 nm and a unit cell with two particles located at $x_1 = 0$, $y_1 = 0$ and $x_2 = 0$, $y_2 = a/4$. The two particles are assumed to be silver nanoshells with silica cores and dimensions identical to those considered in Figure 3, that is, $R_i = 40 \text{ nm}$, $R_o = 50 \text{ nm}$ for particle 1 and R_i = 50 nm, $R_o = 60 \text{ nm}$ for particle 2. For this configuration, the xx and yy components of Re $\{G_{12}\}$ are equal to 0 and Re $\{G_{11}\}$, respectively, as can be seen by examining Figure 2b. Therefore, remembering that the xx and yy components of the lattice sums are independent because the xy terms are negligible near the $\langle 0, \rangle$ ± 1), $\langle \pm 1,0 \rangle$ Rayleigh anomaly (see Figure S2), we can solve eq 3 for each of them separately to predict the response of the array under x- and y-polarized illumination. Under x-polarized illumination, we find that this system behaves exactly as the array considered in Figure 3a-d and therefore supports two lattice resonances with wavelengths determined by $\operatorname{Re}\{\alpha_i^{-1}\}=\operatorname{Re}\{\mathcal{G}_{11}\},$ each of them corresponding to the excitation of an x-polarized dipole in only one of the two particles. On the other hand, when the array is illuminated with y-polarized light, the different value of the yy component of $Re\{G_{12}\}$ results in the array supporting a single lattice resonance with a wavelength determined by $Re\{(\alpha_1 + \alpha_2)^{-1}\} = Re\{\mathcal{G}_{11}\},$ which is associated with the excitation of y-polarized dipoles in particles 1 and 2 with an amplitude ratio α_1/α_2 . Notice that, in contrast to the situation analyzed in Figure 3e-h, in this case, $Re\{G_{12}\} = Re\{G_{11}\}$, which causes the dipoles to oscillate in the same direction.

The numerical results displayed in Figure 4 confirm these predictions. Panels (a,b) show, respectively, the reflectance of the two-particle array under consideration (see inset) and the imaginary part of the dipole induced in each nanoparticle. Examining panel (a), we find that, as expected, the reflectance of the array displays two peaks for x-polarized illumination (solid curve), which becomes a single peak when the polarization of the illumination is changed to the y-axis (dashed curve). The spectral positions of the different peaks are consistent with the predictions obtained from the solution of eq 3. Panel (b) analyzes the corresponding dipoles induced in the different particles. Specifically, red and blue curves are used to plot the imaginary part of the dipole induced, respectively, in particles 1 and 2, normalized to R_0^3 . Clearly, each of the two

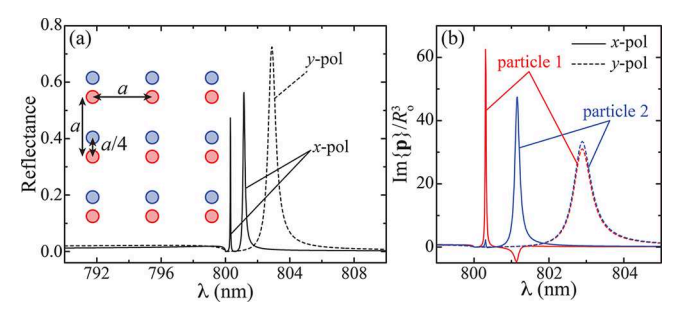


Figure 4. Periodic arrays with complex anisotropic response. (a) Reflectance for an array composed of a square lattice with periodicity a=800 nm and a two-particle unit cell, in which particle 1 (red) is located at the lattice nodes (i.e., $x_1=0$, $y_1=0$) and particle 2 (blue) is placed at $x_2=0$, $y_2=a/4$, as shown in the inset. Both particles are silver nanoshells with silica cores and dimensions identical to those of Figure 3, i.e., $R_i=40$ nm, $R_o=50$ nm for particle 1 and $R_i=50$ nm, $R_o=60$ nm for particle 2. (b) Imaginary part of the dipole induced in particle 1 (red curves) and particle 2 (blue curves) for the lattice considered in panel (a). In both panels, solid and dashed curves correspond to illumination with x- and y-polarized light, respectively.

peaks observed for *x*-polarized illumination (solid curves) corresponds to the excitation of a different particle, while under *y*-polarized illumination (dashed curves), both particles are excited with the induced dipoles oscillating in the same direction.

So far, we have focused on the $\langle 0,\pm 1 \rangle$, $\langle \pm 1,0 \rangle$ Rayleigh anomaly occurring at $\lambda = a$, for which the *xy* component of the lattice sums vanishes, and therefore, the *xx* and *yy* components can be considered separately. However, this is not the case for the $\langle \pm 1,\pm 1 \rangle$, $\langle \pm 1,\mp 1 \rangle$ Rayleigh anomaly located at $\lambda = a/\sqrt{2}$,

for which, as shown in Figure 2c, the xy component of Re $\{G_{ii}\}$ takes values comparable to those of the xx and yy components. A nonvanishing xy component signifies interaction between the x and y components of the induced dipoles and therefore enables the design of more complex responses, 88 in which the induced dipoles do not need to follow the polarization of the external illumination. This can be applied, for instance, to design an array for which the x and y components of the induced dipoles are always equal, regardless of the polarization of the external illumination. To that end, we consider the array described in Figure 5a, consisting of a square lattice of period a = 1300 nm with a two-particle unit cell, in which particle 1 (red) is located at $x_1 = 0$, $y_1 = 0$, whereas particle 2 (blue) is at $x_2 = a/4$, $y_2 = a/4$. Both particles are assumed to be identical silver nanoshells with silica cores and dimensions $R_i = 50 \text{ nm}$, $R_o = 60 \text{ nm}$. For wavelengths near the $\langle \pm 1, \pm 1 \rangle$, $\langle \pm 1, \mp 1 \rangle$ Rayleigh anomaly (i.e., $\lambda = a/\sqrt{2}$), the geometry of the unit cell dictates, as per the results of Figure 2c, that the xx and yy components of Re $\{G_{12}\}$ vanish, whereas the xy one becomes equal to $Re\{G_{11}\}$. Furthermore, for a square lattice, the xy component of \mathcal{G}_{11} is always zero. Therefore, remembering that the imaginary part of the lattice sums are minor on the red side of the Rayleigh anomaly, and thus discarding them, we have

$$\mathcal{G} = \operatorname{Re}\{\mathcal{G}_{11}\} \begin{pmatrix} 1 & 0 & 0 & 1 \\ 0 & 1 & 1 & 0 \\ 0 & 1 & 1 & 0 \\ 1 & 0 & 0 & 1 \end{pmatrix}$$

expressed using the notation in which the dipole reads $\mathbf{p} = (p_{1x}, p_{1y}, p_{2x}, p_{2y})$. Solving eq 3 with this \mathcal{G} , we find that the array under study supports a doubly degenerate lattice resonance,

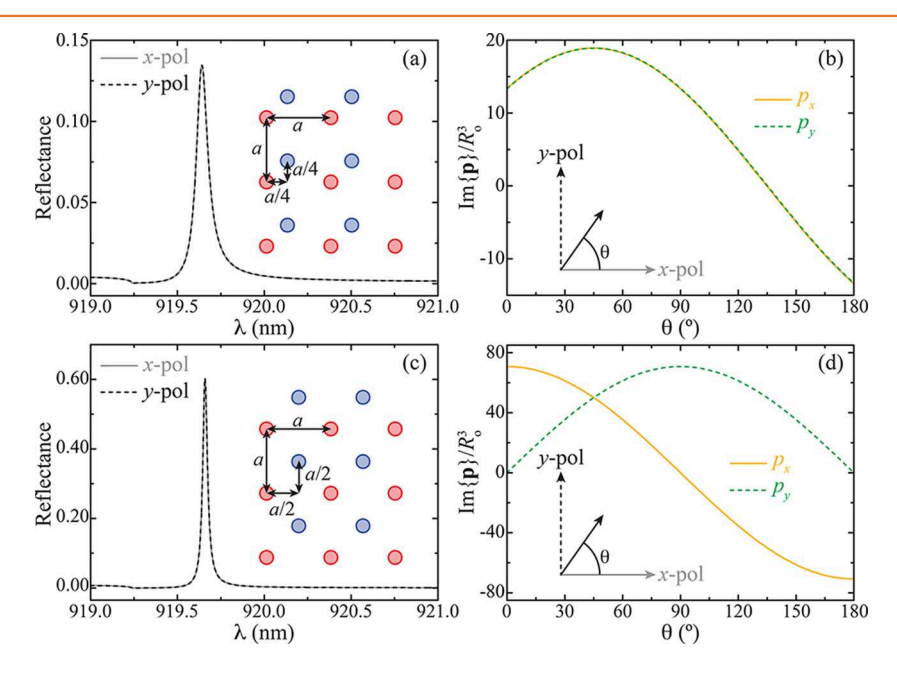


Figure 5. Periodic arrays with response invariant to polarization. (a) Reflectance for an array composed of a square lattice with periodicity a = 1300 nm and a two-particle unit cell (see inset), in which particle 1 (red) is located at the lattice nodes (i.e., $x_1 = 0$, $y_1 = 0$) and particle 2 (blue) is placed at $x_2 = a/4$, $y_2 = a/4$. The gray solid and black dashed curves correspond to illumination with x- and y-polarized light, respectively. Both particles are silver nanoshells with silica cores and dimensions $R_i = 50$ nm, $R_0 = 60$ nm. (b) Imaginary part of the dipole induced in the nanoparticles at resonance (i.e., $\lambda = 919.7$ nm) as a function of the polarization angle of the incident light as indicated by the inset. The yellow and green curves correspond, respectively, to the x and y components of the induced dipole. (c,d) Same as (a,b) but for the case in which particle 2 is placed $x_2 = a/2$, $y_2 = a/2$.

with a wavelength determined by the condition $\operatorname{Re}\{\alpha^{-1}\}=2\operatorname{Re}\{\mathcal{G}_{11}\}$. The corresponding dipole modes are (1,0,0,1) and (0,1,1,0). Then, if the array is illuminated with a field polarized along a direction forming an angle θ with the x-axis, that is, $\mathbf{E}=(\cos\theta,\sin\theta,\cos\theta,\sin\theta)$ in the notation used, the two modes are excited with identical amplitude $\cos\theta+\sin\theta$. This means that the dipole induced in the particles is always proportional to (1,1,1,1), and hence, it has equal x and y components, independent of the polarization angle θ .

Figure 5a shows the reflectance of the array for α -polarized (solid gray curve) and y-polarized (black dashed curve) illumination, calculated numerically using the coupled dipole model. As expected, the array supports a single lattice resonance, irrespective of the light polarization. Panel (b) analyzes the dipole induced in the particles at the lattice resonance (i.e., $\lambda = 919.7 \text{ nm}$) as a function of the polarization angle θ (see inset). Yellow and green curves are used to indicate the imaginary part of the x and y components of the induced dipole. Clearly, as θ is varied, the amplitude of the induced dipole follows the expected $\cos \theta + \sin \theta$ dependence, with the x and y components taking identical values for all angles. This means that the dipole induced in the particles always points in the same direction, regardless of the polarization of the external illumination. The origin of this behavior lies in the coupling arising from the xy component of \mathcal{G}_{12} . Indeed, a similar behavior is found if particle 2 is moved to a position for which the xy component of $Re\{G_{12}\}$ is equal to $-Re\{G_{11}\}$, such as x_2 = a/4, $y_2 = 3a/4$ or $x_2 = 3a/4$, $y_2 = a/4$. However, the different sign of the lattice sum for this configuration changes the coupling amplitude to $-\cos\theta + \sin\theta$ and the induced dipole to (-1,1,-1,1). For the same reasons, moving particle 2 to the center of the unit cell (i.e., $x_2 = a/2$, $y_2 = a/2$), where the xy component $\operatorname{Re}\{\mathcal{G}_{12}\}$ vanishes, is expected to produce a completely different behavior. In this case, we have

$$\mathcal{G} = \operatorname{Re}\{\mathcal{G}_{11}\} \begin{pmatrix} 1 & 0 & 1 & 0 \\ 0 & 1 & 0 & 1 \\ 1 & 0 & 1 & 0 \\ 0 & 1 & 0 & 1 \end{pmatrix}$$

which, upon substitution into eq 3, leads to a solution again consisting in a doubly degenerate lattice resonance located at the same wavelength (i.e., that for which $Re\{\alpha^{-1}\} = 2Re\{\mathcal{G}_{11}\}$). However, in this case, the associated dipole modes are (1,0,1,0) and (0,1,0,1), and therefore, upon illumination with a field E = (cos θ_i sin θ_i cos θ_i sin θ), they are excited with amplitudes cos θ and $\sin \theta$, respectively. This means that the dipole induced in the particles is proportional to E, and its direction therefore exactly follows the polarization of the field. This behavior is clearly corroborated by the numerical results shown in panels (c,d) of Figure 5. The former displays the reflectance of this array, confirming the presence of a lattice resonance for both xand y-polarized illumination with the same wavelength as that of the array of panel (a). Panel (d), on the other hand, shows the behavior of the induced dipole, verifying that it exactly follows the polarization of the external field.

All of the systems studied so far involve arrays with unit cells containing two particles. However, the hybridization approach described here applies equally to systems with arbitrary unit cells. An interesting example of an array with a three-particle unit cell is the Lieb lattice, ⁸³ depicted in the right inset of Figure 6a, which is being extensively studied due to its unusual

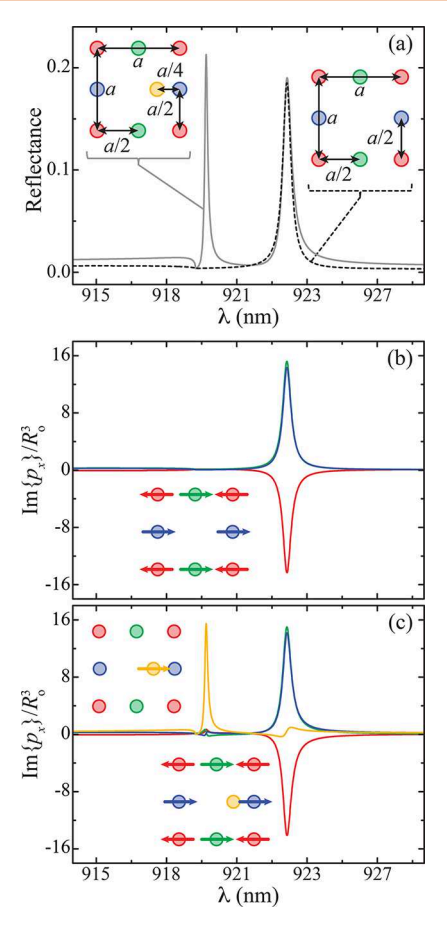


Figure 6. Periodic arrays with three- and four-particle unit cells. (a) Reflectance for two different arrays composed of a square lattice with periodicity $a=1300\,\mathrm{nm}$ and a three- (black dashed curve) or four-particle unit cell (gray solid curve), arranged as shown in the insets. In both cases, all particles are identical silver nanoshells with silica cores and dimensions $R_i=50\,\mathrm{nm}$, $R_o=80\,\mathrm{nm}$. The incident light is polarized along the x-axis. (b,c) Imaginary part of the dipole induced in each of the nanoparticles for the arrays with three- (b) and four-particle (c) unit cells. The curves are color-coded to match the insets, which show the direction of the dipoles induced at each resonance.

topological properties that lead to extraordinary optical responses. So It consists of a square array with periodicity a=1300 nm and a unit cell containing three particles located at $x_1=0$, $y_1=0$ (red particle), $x_2=0$, $y_2=a/2$ (blue particle), and $x_3=a/2$, $y_3=0$ (green particle). All of the particles are taken to be identical silver nanoshells with silica cores and dimensions $R_i=50$ nm, $R_o=80$ nm. Near the $\langle \pm 1,\pm 1 \rangle$, $\langle \pm 1,\mp 1 \rangle$ Rayleigh anomaly (i.e., $\lambda=a/\sqrt{2}$), the xy component of $\text{Re}\{\mathcal{G}_{ij}\}$ vanishes for all values of i and j, as can be seen in Figure 2c. Therefore, assuming x-polarized illumination, we only need to consider the xx component of \mathcal{G} , which reduces to the 3×3 matrix

$$\mathcal{G} = \text{Re}\{\mathcal{G}_{11}\} \begin{pmatrix} 1 & -1 & -1 \\ -1 & 1 & 1 \\ -1 & 1 & 1 \end{pmatrix}$$

where we use the notation $\mathbf{p} = (p_{1xy}p_{2xy}p_{3x})$. Introducing this expression into eq 3 and solving it, we find that the system supports a single lattice resonance, whose wavelength satisfies $\operatorname{Re}\{\alpha^{-1}\}=3\operatorname{Re}\{\mathcal{G}_{11}\}$. The associated dipole mode is (-1,1,1),

meaning that, while the dipoles induced in particles 2 and 3 oscillate in the same direction, that of particle 1 does so in the opposite direction. This is corroborated by the numerical calculations shown in Figure 6a,b, which display, respectively, the reflectance of the array (dashed black curve) and the imaginary part of the dipole induced in the different particles. The results of the latter are color-coded according to the inset.

It is possible to add a fourth particle to this array at a position such that it does not interact with any of the three original particles. There are, indeed, four positions within the unit cell for which this happens, all of them characterized by the fact that the xx, yy, and xy components of $Re\{\mathcal{G}_{14}\}$, $Re\{\mathcal{G}_{24}\}$, and $Re\{\mathcal{G}_{34}\}$ vanish. These positions correspond to the points for which the dashed lines of the upper panel of Figure 2c intersect those of the lower one. When particle 4 is placed at one of these positions, \mathcal{G} becomes

$$\mathcal{G} = \operatorname{Re}\{\mathcal{G}_{11}\} \begin{pmatrix} 1 & -1 & -1 & 0 \\ -1 & 1 & 1 & 0 \\ -1 & 1 & 1 & 0 \\ 0 & 0 & 0 & 1 \end{pmatrix}$$

using the notation $\mathbf{p} = (p_{1x}p_{2x}p_{3x}p_{3x}p_{4x})$. Therefore, this new array supports, in addition to the lattice resonance of the threeparticle array, a new mode at a wavelength $Re\{\alpha^{-1}\}=Re\{\mathcal{G}_{11}\}$. Clearly, the dipole associated with this new lattice resonance is (0,0,0,1), which, as anticipated, involves only the excitation of particle 4. The two predicted resonances are visible in the reflectance spectrum of Figure 6a (gray solid curve), which is calculated for particle 4 located at $x_4 = 3a/4$, $y_4 = a/2$, as indicated in the left inset. The corresponding induced dipoles are analyzed in panel (c), where the different colors represent the different particles in the unit cell. The left peak involves the exclusive excitation of particle 4, whereas the right one corresponds to the excitation pattern of the lattice resonance of the three-particle array (cf. panels (b,c)). All of these results show the extraordinary potential of multiparticle arrays to support engineered lattice resonances that allow for the selective excitation of different groups of particles in the unit

CONCLUSIONS

In summary, we have presented a detailed analysis of the optical response of periodic arrays with unit cells containing an arbitrary number of nanoparticles based on the plasmon hybridization approach. We can think of these systems as the superposition of a number of identical single-particle arrays, one per particle in the unit cell, which are displaced in the plane in which they all lie. By utilizing this description, we have shown that the lattice resonances supported by these multiparticle arrays can be understood from the hybridization of the lattice resonances of the individual single-particle arrays, in the same way as the plasmonic response of complex nanostructures arises from the hybridization of the plasmons supported by their constituents. However, lattice resonances are extended excitations, and their interaction is therefore governed by far-field coupling, in sharp contrast with the localized plasmons supported by particles, which interact primarily through near-field coupling. This leads to the much richer hybridization scenario that we have described in this work. Specifically, we have shown that the sign of the

interaction between lattice resonances, as well as its strength, is determined by the relative position of the corresponding particles within the unit cell. Therefore, it is possible to control the interaction, and even cancel it, by placing the particles at appropriate positions. We have exploited this behavior to design different arrays with engineered optical responses. In particular, we have studied a two-particle array, which, when the relative position of the particles is chosen to suppress the interaction, supports two different lattice resonances, each involving the excitation of only one of the particles. If, on the other hand, the relative position is selected to maximize the coupling, the array displays a single lattice resonance with the particles being excited in the same or opposite directions, depending on the sign of the interaction. Furthermore, the control of the interaction between the lattice resonances allows for the design of arrays with responses either invariant to the polarization of the incident light or strongly dependent on it. We have also investigated three- and four-particle arrays for which, by controlling the arrangement of the unit cell, it is possible to tailor the interaction to produce lattice resonances that selectively excite different groups of particles within the unit cell. It is important to remark that, although we have focused on periodic arrays built from metallic nanoparticles, the results and methodology presented here can be directly applied to arrays composed of other photonic elements, including dielectric nanoparticles and atoms. Indeed, the dipolar nature of atomic transitions make two-dimensional atomic arrays ideal platforms to explore the concepts introduced here. 72-74 The results of this work serve to advance our understanding of the behavior of lattice resonances and provide a methodology to design periodic arrays of nanostructures with engineered optical responses.

METHODS

Lattice Sums. The lattice sums appearing in eq 2 are defined as

$$\mathcal{G}_{ij}(\mathbf{k}_{\parallel}) = \sum_{\nu} \mathbf{G}_{ij,\nu0} e^{-i\mathbf{k}_{\parallel} \mathbf{T}_{\nu}}$$

where the prime on the sum indicates that the term $\nu=0$ is excluded from it when i=j. It is important to notice that the dipole—dipole interaction tensor $\mathbf{G}_{ij\nu0}$ contains terms that decay with distance as $|\mathbf{T}_{\nu}+\mathbf{r}_i-\mathbf{r}_j|^{-1}$, $|\mathbf{T}_{\nu}+\mathbf{r}_i-\mathbf{r}_j|^{-2}$, and $|\mathbf{T}_{\nu}+\mathbf{r}_i-\mathbf{r}_j|^{-3}$, corresponding, respectively, to the far-, mid-, and near-field coupling. At wavelengths near a Rayleigh anomaly, the lattice sum is dominated by the far-field coupling term, which produces a divergent contribution. The reason is that, while the far-field coupling decays with the inverse of the distance, the number of array sites included in the lattice sum increases with its square, thus leading to a divergent contribution that dominates over those arising from the mid- and near-field coupling terms.

The lattice sum defined above can be efficiently calculated using Ewald's method. However, we can gain some insight by rewriting $\mathcal{G}_{ij}(\mathbf{k}_{\parallel})$, using the Weyl identity, as

$$\mathcal{G}_{ij}(\mathbf{k}_{\parallel}) = \lim_{z \to 0} \sum_{\nu} e^{-i\mathbf{k}_{\parallel} \mathbf{T}_{\nu}} (k^2 + \nabla \nabla) \frac{i}{2\pi} \int \frac{d\mathbf{k}_{\parallel}'}{k_{z}'} e^{i\mathbf{k}_{\parallel}'' (\mathbf{T}_{\nu} + \mathbf{r}_{i} - \mathbf{r}_{j})} e^{ik_{z}'|z|}$$

This expression can be further simplified by noting that, due to the periodicity

$$\sum_{\nu} e^{i(\mathbf{k}_{\parallel}^{\prime} - \mathbf{k}_{\parallel}) \cdot \mathbf{I}_{\nu}^{\prime}} = \frac{4\pi^{2}}{A} \sum_{\mathbf{q}} \delta(\mathbf{k}_{\parallel}^{\prime} - \mathbf{k}_{\parallel} - \mathbf{q})$$

where A is the area of the unit cell and \mathbf{q} are the reciprocal lattice vectors. Using this relation, we have

$$\mathcal{G}_{ij}(\mathbf{k}_{\parallel}) = \frac{2\pi i}{A} \sum_{\mathbf{q}} \begin{pmatrix} k^{2} - (q_{x} + k_{x})^{2} & - (q_{x} + k_{x})(q_{y} + k_{y}) & - (q_{x} + k_{x})k_{z\mathbf{q}} \\ - (q_{y} + k_{y})(q_{x} + k_{x}) & k^{2} - (q_{y} + k_{y})^{2} & - (q_{y} + k_{y})k_{z\mathbf{q}} \\ - k_{z\mathbf{q}}(q_{x} + k_{x}) & - k_{z\mathbf{q}}(q_{y} + k_{y}) & k^{2} - k_{z\mathbf{q}}^{2} \end{pmatrix} \frac{e^{i(\mathbf{q} + k_{\parallel}) \cdot (\mathbf{r}_{i} - \mathbf{r}_{i})}}{k_{z\mathbf{q}}} - i \frac{\delta_{ij}}{2\pi} \int \frac{d\mathbf{k}_{\parallel}'}{k_{z}'} \begin{pmatrix} k^{2} - k_{x}'^{2} & - k_{x}'k_{y}' & - k_{x}'k_{z}' \\ - k_{y}'k_{x}' & k^{2} - k_{y}'^{2} & - k_{y}'k_{z}' \\ - k_{z}'k_{x}' & - k_{z}'k_{y}' & k^{2} - k_{z}'^{2} \end{pmatrix}$$

$$(4)$$

where $k_{z\mathbf{q}}=\sqrt{k^2-(\mathbf{q}+\mathbf{k}_{\parallel})^2}$. The vanishing of this quantity determines the existence of the Rayleigh anomalies. For instance, for a square lattice of periodicity a, the reciprocal lattice vectors have components $q_x=2\pi m/a$ and $q_y=2\pi n/a$, and therefore $\lambda_{m,n}=2\pi/\sqrt{(2\pi m/a+k_x)^2+(2\pi n/a+k_y)^2}$, where m and n are integers. This expression reduces to $\lambda_{m,n}=a/\sqrt{m^2+n^2}$ for normal incidence ($\mathbf{k}_{\parallel}=0$), which explains the degeneracy of the Rayleigh anomalies considered in this work. Such degeneracy is lifted for $\mathbf{k}_{\parallel}\neq0$, resulting in a much larger set of Rayleigh anomalies.

On the red side of a Rayleigh anomaly, the associated reciprocal lattice vector satisfies $(\mathbf{q} + \mathbf{k}_{\parallel})^2 > k^2$, and the corresponding $k_{z\mathbf{q}}$ therefore becomes purely imaginary. This makes $\mathcal{G}_{ij}(\mathbf{k}_{\parallel})$ predominantly real in these parts of the spectrum, as shown in Figure S1 of the Supporting Information. There, we plot the real and imaginary parts of \mathcal{G}_{ij} as a function of wavelength for different cases relevant to the systems investigated in this work.

Examining eq 4 closely, we notice that for wavelengths on the red side of the of the Rayleigh anomalies, the zeros of the different components of $\text{Re}\{\mathcal{G}_{ij}\}$ appear for the relative positions between particle i and j that satisfy the condition

$$\sum_{\mathbf{q}} f(\mathbf{q}, \mathbf{k}_{\parallel}) \cos[(\mathbf{q} + \mathbf{k}_{\parallel}) \cdot (\mathbf{r}_i - \mathbf{r}_j)] = 0$$
(5)

where $f(\mathbf{q},\mathbf{k}_{\parallel})$ is the corresponding element of the matrix of eq 4, and the sum runs over all of the reciprocal lattice vectors associated with the corresponding Rayleigh anomaly. For normal incidence $(\mathbf{k}_{\parallel}=0)$, these zeros are indicated with black dashed lines in Figure 2, as well as in Figures S2, S4, and S5. When the wavelength increases, and therefore moves away from the corresponding Rayleigh anomalies, the lines indicating the zeros of $\text{Re}\{\mathcal{G}_{ij}\}$ become more complicated, but the same general features are preserved, as shown in Figure S3. For tilted incidence (i.e., $\mathbf{k}_{\parallel} \neq 0$), in addition of the breaking of the degeneracy of the Rayleigh anomalies discussed above, the solutions of eq 5 become more involved, leading to more complex patterns than those obtained for normal incidence.

Calculation of Nanoshell Polarizability. In all of the examples discussed in this work, we calculate the polarizability of the different nanoshells from the dipolar Mie scattering coefficient⁸⁷ as $\alpha = 3/(2k^3)$ t_i^E , where

$$t_1^{\mathrm{E}} = -\frac{j_1(\rho_0)a_1 - [\rho_0 j_1(\rho_0)]'b_1}{h_1^{(+)}(\rho_0)a_1 - [\rho_0 h_1^{(+)}(\rho_0)]'b_1}$$

Here, $j_1(x)$ and $h_1^{(+)}(x)$ are the spherical Bessel and Hankel functions of order 1, the prime denotes differentiation with respect to the argument, and

$$\begin{split} a_1 &= \varepsilon_o [\rho_j j_1(\rho_1)]' A_1 - \varepsilon_j j_1(\rho_1) B_1 \\ b_1 &= \varepsilon_o^2 [\rho_j j_1(\rho_1)]' C_1 - \varepsilon_o \varepsilon_j j_1(\rho_1) D_1 \\ A_1 &= j_1(\rho_2) [\rho_3 h_1^{(+)}(\rho_3)]' - h_1^{(+)}(\rho_2) [\rho_3 j_1(\rho_3)]' \\ B_1 &= [\rho_2 j_1(\rho_2)]' [\rho_3 h_1^{(+)}(\rho_3)]' - [\rho_2 h_1^{(+)}(\rho_2)]' [\rho_3 j_1(\rho_3)]' \\ C_1 &= j_1(\rho_2) h_1^{(+)}(\rho_3) - h_1^{(+)}(\rho_2) j_1(\rho_3) \\ D_1 &= [\rho_2 j_1(\rho_2)]' h_1^{(+)}(\rho_3) - [\rho_2 h_1^{(+)}(\rho_2)]' j_1(\rho_3) \end{split}$$

In these expressions, $\rho_1 = \sqrt{\varepsilon_i} \, k R_i$, $\rho_2 = \sqrt{\varepsilon_o} \, k R_i$, $\rho_3 = \sqrt{\varepsilon_o} \, k R_o$, and $\rho_0 = k R_o$, where R_i and R_o are, respectively, the inner and outer radius, whereas ε_i and ε_o are the dielectric function of the materials in the core and in the shell. In our case, these materials are, respectively, silica and silver, whose dielectric functions we take from tabulated data. 93,94

ASSOCIATED CONTENT

S Supporting Information

The Supporting Information is available free of charge on the ACS Publications website at DOI: 10.1021/acsnano.7b08206.

Analysis of the dependence of the lattice sums on the wavelength; more examples of the lattice sums corresponding to higher-order Rayleigh anomalies; analysis of the accuracy of the coupled dipole model through the comparison with full-wave calculations obtained using the finite element method approach (PDF)

AUTHOR INFORMATION

Corresponding Author

*E-mail: manjavacas@unm.edu.

ORCID

Alejandro Manjavacas: 0000-0002-2379-1242

Notes

The authors declare no competing financial interest.

ACKNOWLEDGMENTS

This work has been sponsored by the U.S. National Science Foundation (Grant ECCS-1710697). We acknowledge the UNM Center for Advanced Research Computing for computational resources used in this work. We are also grateful to Ms. Lauren Zundel for her critical reading of the manuscript.

REFERENCES

(1) Maier, S. A. Plasmonics: Fundamentals and Applications; Springer: New York, 2007.

(2) Catchpole, K. R.; Polman, A. Plasmonic Solar Cells. *Opt. Express* **2008**, *16*, 21793–21800.

- (3) Atwater, H. A.; Polman, A. Plasmonics for Improved Photovoltaic Devices. *Nat. Mater.* **2010**, *9*, 205–213.
- (4) Baffou, G.; Quidant, R. Nanoplasmonics for Chemistry. Chem. Soc. Rev. 2014, 43, 3898-3907.
- (5) Brongersma, M. L.; Halas, N. J.; Nordlander, P. Plasmon-Induced Hot Carrier Science and Technology. *Nat. Nanotechnol.* **2015**, *10*, 25–34.
- (6) Xu, H.; Bjerneld, E. J.; Käll, M.; Börjesson, L. Spectroscopy of Single Hemoglobin Molecules by Surface Enhanced Raman Scattering. *Phys. Rev. Lett.* **1999**, 83, 4357–4360.
- (7) Anker, J. N.; Hall, W. P.; Lyandres, O.; Shah, N. C.; Zhao, J.; Van Duyne, R. P. Biosensing with Plasmonic Nanosensors. *Nat. Mater.* **2008**, 7, 442–453.
- (8) Lozano, G.; Louwers, D. J.; Rodriguez, S. R. K.; Murai, S.; Jansen, O. T. A.; Verschuuren, M. A.; Gomez Rivas, J. Plasmonics for Solid-State Lighting: Enhanced Excitation and Directional Emission of Highly Efficient Light Sources. *Light: Sci. Appl.* **2013**, *2*, e66.
- (9) Yang, A.; Odom, T. W. Breakthroughs in Photonics 2014: Advances in Plasmonic Nanolasers. *IEEE Photonics J.* **2015**, *7*, 1–6.
- (10) Liu, K.; Li, N.; Sadana, D. K.; Sorger, V. J. Integrated Nanocavity Plasmon Light Sources for On-Chip Optical Interconnects. ACS Photonics 2016, 3, 233–242.
- (11) Halas, N. J.; Lal, S.; Chang, W.; Link, S.; Nordlander, P. Plasmons in Strongly Coupled Metallic Nanostructures. *Chem. Rev.* **2011**, *111*, 3913–3961.
- (12) Lassiter, J. B.; Sobhani, H.; Fan, J. A.; Kundu, J.; Capasso, F.; Nordlander, P.; Halas, N. J. Fano Resonances in Plasmonic Nanoclusters: Geometrical and Chemical Tunability. *Nano Lett.* **2010**, *10*, 3184–3189.
- (13) Prodan, E.; Radloff, C.; Halas, N. J.; Nordlander, P. Hybridization Model for the Plasmon Response of Complex Nanostructures. *Science* **2003**, 302, 419–422.
- (14) Nordlander, P.; Oubre, C.; Prodan, E.; Li, K.; Stockman, M. I. Plasmon Hybridizaton in Nanoparticle Dimers. *Nano Lett.* **2004**, *4*, 899–903.
- (15) Yang, S.-C.; Kobori, H.; He, C.-L.; Lin, M.-H.; Chen, H.-Y.; Li, C.; Kanehara, M.; Teranishi, T.; Gwo, S. Plasmon Hybridization in Individual Gold Nanocrystal Dimers: Direct Observation of Bright and Dark Modes. *Nano Lett.* **2010**, *10*, 632–637.
- (16) Lassiter, J. B.; Aizpurua, J.; Hernandez, L. I.; Brandl, D. W.; Romero, I.; Lal, S.; Hafner, J. H.; Nordlander, P.; Halas, N. J. Close Encounters Between Two Nanoshells. *Nano Lett.* **2008**, *8*, 1212–1218.
- (17) Bardhan, R.; Grady, N. K.; Ali, T.; Halas, N. J. Metallic Nanoshells with Semiconductor Cores: Optical Characteristics Modified by Core Medium Properties. ACS Nano 2010, 4, 6169–6179.
- (18) Ramadurgam, S.; Yang, C. Semiconductor-Metal-Semiconductor Core-Multishell Nanowires as Negative-Index Metamaterial in Visible Domain. Sci. Rep. 2015, 4, 4931.
- (19) Vogel, N.; Fischer, J.; Mohammadi, R.; Retsch, M.; Butt, H.-J.; Landfester, K.; Weiss, C. K.; Kreiter, M. Plasmon Hybridization in Stacked Double Crescents Arrays Fabricated by Colloidal Lithography. *Nano Lett.* **2011**, *11*, 446–454.
- (20) Fischer, J.; Vogel, N.; Mohammadi, R.; Butt, H.-J.; Landfester, K.; Weiss, C. K.; Kreiter, M. Plasmon Hybridization and Strong Near-Field Enhancements in Opposing Nanocrescent Dimers with Tunable Resonances. *Nanoscale* **2011**, *3*, 4788–4797.
- (21) Hao, F.; Nordlander, P.; Burnett, M. T.; Maier, S. A. Enhanced Tunability and Linewidth Sharpening of Plasmon Resonances in Hybridized Metallic Ring/Disk Nanocavities. *Phys. Rev. B: Condens. Matter Mater. Phys.* **2007**, *76*, 245417.
- (22) Chang, Y.-C.; Wang, S.-M.; Chung, H.-C.; Tseng, C.-B.; Chang, S.-H. Observation of Absorption-Dominated Bonding Dark Plasmon Mode from Metal-Insulator-Metal Nanodisk Arrays Fabricated by Nanospherical-Lens Lithography. ACS Nano 2012, 6, 3390–3396.

(23) Yankovich, A. B.; Verre, R.; Olsén, E.; Persson, A. E. O.; Trinh, V.; Dovner, G.; Käll, M.; Olsson, E. Multidimensional Hybridization of Dark Surface Plasmons. *ACS Nano* **2017**, *11*, 4265–4274.

- (24) Yan, H.; Xia, F.; Li, Z.; Avouris, P. Plasmonics of Coupled Graphene Micro-Structures. New J. Phys. 2012, 14, 125001.
- (25) Christensen, J.; Manjavacas, A.; Thongrattanasiri, S.; Koppens, F. H. L.; García de Abajo, F. J. Graphene Plasmon Waveguiding and Hybridization in Individual and Paired Nanoribbons. *ACS Nano* **2012**, *6*, 431–440.
- (26) Fang, Z.; Thongrattanasiri, S.; Schlather, A.; Liu, Z.; Ma, L.; Wang, Y.; Ajayan, P. M.; Nordlander, P.; Halas, N. J.; García de Abajo, F. J. Gated Tunability and Hybridization of Localized Plasmons in Nanostructured Graphene. *ACS Nano* **2013**, *7*, 2388–2395.
- (27) Wang, W.; Christensen, T.; Jauho, A.-P.; Thygesen, K. S.; Wubs, M.; Mortensen, N. A. Plasmonic Eigenmodes in Individual and Bow-Tie Graphene Nanotriangles. Sci. Rep. 2015, 5, 9535.
- (28) Luk'yanchuk, B.; Zheludev, N. I.; Maier, S. A.; Halas, N. J.; Nordlander, P.; Giessen, H.; Chong, C. The Fano Resonance in Plasmonic Nanostructures and Metamaterials. *Nat. Mater.* **2010**, *9*, 707–715.
- (29) Lovera, A.; Gallinet, B.; Nordlander, P.; Martin, O. J. Mechanisms of Fano Resonances in Coupled Plasmonic Systems. *ACS Nano* **2013**, *7*, 4527–4536.
- (30) Hajebifard, A.; Berini, P. Fano Resonances in Plasmonic Heptamer Nano-Hole Arrays. Opt. Express 2017, 25, 18566–18580.
- (31) Alonso-Gonzalez, P.; Schnell, M.; Sarriugarte, P.; Sobhani, H.; Wu, C.; Arju, N.; Khanikaev, A.; Golmar, F.; Albella, P.; Arzubiaga, L.; Casanova, F.; Hueso, L. E.; Nordlander, P.; Shvets, G.; Hillenbrand, R. Real-Space Mapping of Fano Interference in Plasmonic Metamolecules. *Nano Lett.* **2011**, *11*, 3922–3926.
- (32) Hentschel, M.; Dregely, D.; Vogelgesang, R.; Giessen, H.; Liu, N. Plasmonic Oligomers: The Role of Individual Particles in Collective Behavior. *ACS Nano* **2011**, *5*, 2042–2050.
- (33) Dregely, D.; Hentschel, M.; Giessen, H. Excitation and Tuning of Higher-Order Fano Resonances in Plasmonic Oligomer Clusters. *ACS Nano* **2011**, *5*, 8202–8211.
- (34) Frimmer, M.; Coenen, T.; Koenderink, A. F. Signature of a Fano Resonance in a Plasmonic Metamolecule's Local Density of Optical States. *Phys. Rev. Lett.* **2012**, *108*, 077404.
- (35) Koh, A. L.; Bao, K.; Khan, I.; Smith, W. E.; Kothleitner, G.; Nordlander, P.; Maier, S. A.; McComb, D. W. Electron Energy-Loss Spectroscopy (EELS) of Surface Plasmons in Single Silver Nanoparticles and Dimers: Influence of Beam Damage and Mapping of Dark Modes. ACS Nano 2009, 3, 3015–3022.
- (36) Ögüt, B.; Vogelgesang, R.; Sigle, W.; Talebi, N.; Koch, C. T.; van Aken, P. A. Hybridized Metal Slit Eigenmodes as an Illustration of Babinet's Principle. ACS Nano 2011, 5, 6701–6706.
- (37) Quillin, S. C.; Cherqui, C.; Montoni, N. P.; Li, G.; Camden, J. P.; Masiello, D. J. Imaging Plasmon Hybridization in Metal Nanoparticle Aggregates with Electron Energy-Loss Spectroscopy. *J. Phys. Chem. C* **2016**, *120*, 20852–20859.
- (38) Bellido, E. P.; Zhang, Y.; Manjavacas, A.; Nordlander, P.; Botton, G. A. Plasmonic Coupling of Multipolar Edge Modes and the Formation of Gap Modes. *ACS Photonics* **2017**, *4*, 1558–1565.
- (39) Guo, H.; Liu, N.; Fu, L.; Meyrath, T. P.; Zentgraf, T.; Schweizer, H.; Giessen, H. Resonance Hybridization in Double Split-Ring Resonator Metamaterials. *Opt. Express* **2007**, *15*, 12095–12101.
- (40) Lobet, M.; Lard, M.; Sarrazin, M.; Deparis, O.; Henrard, L. Plasmon Hybridization in Pyramidal Metamaterials: A Route Towards Ultra-Broadband Absorption. *Opt. Express* **2014**, *22*, 12678–12690.
- (41) Hajisalem, G.; Ahmed, A.; Pang, Y.; Gordon, R. Plasmon Hybridization for Enhanced Nonlinear Optical Response. *Opt. Express* **2012**, *20*, 29923–29930.
- (42) Metzger, B.; Hentschel, M.; Giessen, H. Ultrafast Nonlinear Plasmonic Spectroscopy: From Dipole Nanoantennas to Complex Hybrid Plasmonic Structures. ACS Photonics 2016, 3, 1336–1350.
- (43) Auguié, B.; Alonso-Gómez, J. L.; Guerrero-Martínez, A.; Liz-Marzán, L. M. Fingers Crossed: Optical Activity of a Chiral Dimer of Plasmonic Nanorods. J. Phys. Chem. Lett. 2011, 2, 846–851.

(44) Hentschel, M.; Ferry, V. E.; Alivisatos, A. P. Optical Rotation Reversal in the Optical Response of Chiral Plasmonic Nanosystems: The Role of Plasmon Hybridization. *ACS Photonics* **2015**, *2*, 1253–1259

- (45) Zhao, L.; Kelly, K. L.; Schatz, G. C. The Extinction Spectra of Silver Nanoparticle Arrays: Influence of Array Structure on Plasmon Resonance Wavelength and Width. J. Phys. Chem. B 2003, 107, 7343—7350
- (46) García de Abajo, F. J. Colloquium: Light Scattering by Particle and Hole Arrays. *Rev. Mod. Phys.* **2007**, *79*, 1267–1290.
- (47) Auguié, B.; Barnes, W. L. Collective Resonances in Gold Nanoparticle Arrays. *Phys. Rev. Lett.* **2008**, *101*, 143902.
- (48) Kravets, V. G.; Schedin, F.; Grigorenko, A. N. Extremely Narrow Plasmon Resonances Based on Diffraction Coupling of Localized Plasmons in Arrays of Metallic Nanoparticles. *Phys. Rev. Lett.* **2008**, 101, 087403.
- (49) Yang, A.; Hryn, A. J.; Bourgeois, M. R.; Lee, W.-K.; Hu, J.; Schatz, G. C.; Odom, T. W. Programmable and Reversible Plasmon Mode Engineering. *Proc. Natl. Acad. Sci. U. S. A.* **2016**, *113*, 14201–14206.
- (50) Vecchi, G.; Giannini, V.; Gómez Rivas, J. Surface Modes in Plasmonic Crystals Induced by Diffractive Coupling of Nanoantennas. *Phys. Rev. B: Condens. Matter Mater. Phys.* **2009**, 80, 201401.
- (51) Giannini, V.; Vecchi, G.; Gómez Rivas, J. Lighting Up Multipolar Surface Plasmon Polaritons by Collective Resonances in Arrays of Nanoantennas. *Phys. Rev. Lett.* **2010**, *105*, 266801.
- (52) Teperik, T. V.; Degiron, A. Design Strategies to Tailor the Narrow Plasmon-Photonic Resonances in Arrays of Metallic Nanoparticles. *Phys. Rev. B: Condens. Matter Mater. Phys.* **2012**, *86*, 245425.
- (53) Almpanis, E.; Papanikolaou, N.; Auguié, B.; Tserkezis, C.; Stefanou, N. Diffractive Chains of Plasmonic Nanolenses: Combining Near-Field Focusing and Collective Enhancement Mechanisms. *Opt. Lett.* 2012, 37, 4624–4626.
- (54) Rodriguez, S. R. K.; Lozano, G.; Verschuuren, M. A.; Gomes, R.; Lambert, K.; De Geyter, B.; Hassinen, A.; Van Thourhout, D.; Hens, Z.; Gomez Rivas, J. Quantum Rod Emission Coupled to Plasmonic Lattice Resonances: A Collective Directional Source of Polarized Light. Appl. Phys. Lett. 2012, 100, 111103.
- (55) Zhou, W.; Dridi, M.; Suh, J. Y.; Kim, C. H.; Co, D. T.; Wasielewski, M. R.; Schatz, G. C.; Odom, T. W. Lasing Action in Strongly Coupled Plasmonic Nanocavity Arrays. *Nat. Nanotechnol.* **2013**, *8*, 506–511.
- (56) Lozano, G.; Grzela, G.; Verschuuren, M. A.; Ramezani, M.; Rivas, J. G. Tailor-Made Directional Emission in Nanoimprinted Plasmonic-Based Light-Emitting Devices. *Nanoscale* **2014**, *6*, 9223–9229.
- (57) Schokker, A. H.; Koenderink, A. F. Lasing at the Band Edges of Plasmonic Lattices. *Phys. Rev. B: Condens. Matter Mater. Phys.* **2014**, 90, 155452.
- (58) Teperik, T. V.; Degiron, A. Control of Plasmonic Crystal Light Emission. J. Opt. Soc. Am. B 2014, 31, 223–228.
- (59) Ramezani, M.; Lozano, G.; Verschuuren, M. A.; Gómez-Rivas, J. Modified Emission of Extended Light Emitting Layers by Selective Coupling to Collective Lattice Resonances. *Phys. Rev. B: Condens. Matter Mater. Phys.* **2016**, 94, 125406.
- (60) Olson, J.; Manjavacas, A.; Basu, T.; Huang, D.; Schlather, A. E.; Zheng, B.; Halas, N. J.; Nordlander, P.; Link, S. High Chromaticity Aluminum Plasmonic Pixels for Active Liquid Crystal Displays. ACS Nano 2016, 10, 1108–1117.
- (61) Zakharko, Y.; Held, M.; Graf, A.; Rödlmeier, T.; Eckstein, R.; Hernandez-Sosa, G.; Hähnlein, B.; Pezoldt, J.; Zaumseil, J. Surface Lattice Resonances for Enhanced and Directional Electroluminescence at High Current Densities. ACS Photonics 2016, 3, 2225–2230.
- (62) Cotrufo, M.; Osorio, C. I.; Koenderink, A. F. Spin-Dependent Emission from Arrays of Planar Chiral Nanoantennas Due to Lattice and Localized Plasmon Resonances. *ACS Nano* **2016**, *10*, 3389–3397. (63) Hakala, T. K.; Rekola, H. T.; Väkeväinen, A. I.; Martikainen, J.-

P.; Nečada, M.; Moilanen, A. J.; Törmä, P. Lasing in Dark and Bright

- Modes of a Finite-Sized Plasmonic Lattice. Nat. Commun. 2017, 8, 13687
- (64) Wang, D.; Yang, A.; Wang, W.; Hua, Y.; Schaller, R. D.; Schatz, G. C.; Odom, T. W. Band-Edge Engineering for Controlled Multi-Modal Nanolasing in Plasmonic Superlattices. *Nat. Nanotechnol.* **2017**, 12 889
- (65) Thackray, B. D.; Kravets, V. G.; Schedin, F.; Auton, G.; Thomas, P. A.; Grigorenko, A. N. Narrow Collective Plasmon Resonances in Nanostructure Arrays Observed at Normal Light Incidence for Simplified Sensing in Asymmetric Air and Water Environments. *ACS Photonics* **2014**, *1*, 1116–1126.
- (66) Yang, A.; Huntington, M. D.; Cardinal, M. F.; Masango, S. S.; Van Duyne, R. P.; Odom, T. W. Hetero-oligomer Nanoparticle Arrays for Plasmon-Enhanced Hydrogen Sensing. *ACS Nano* **2014**, *8*, 7639–7647
- (67) Liu, N.; Mesch, M.; Weiss, T.; Hentschel, M.; Giessen, H. Infrared Perfect Absorber and its Application as Plasmonic Sensor. *Nano Lett.* **2010**, *10*, 2342–2348.
- (68) Thongrattanasiri, S.; Koppens, F. H. L.; García de Abajo, F. J. Complete Optical Absorption in Periodically Patterned Graphene. *Phys. Rev. Lett.* **2012**, *108*, 047401.
- (69) Ra'di, Y.; Asadchy, V. S.; Kosulnikov, S. U.; Omelyanovich, M. M.; Morits, D.; Osipov, A. V.; Simovski, C. R.; Tretyakov, S. A. Full Light Absorption in Single Arrays of Spherical Nanoparticles. *ACS Photonics* **2015**, *2*, 653–660.
- (70) Väkeväinen, A. I.; Moerland, R. J.; Rekola, H. T.; Eskelinen, A.-P.; Martikainen, J.-P.; Kim, D.-H.; Törmä, P. Plasmonic Surface Lattice Resonances at the Strong Coupling Regime. *Nano Lett.* **2014**, *14*, 1721–1727.
- (71) Todisco, F.; Esposito, M.; Panaro, S.; De Giorgi, M.; Dominici, L.; Ballarini, D.; Fernández-Domínguez, A. I.; Tasco, V.; Cuscunà, M.; Passaseo, A.; Ciracì, C.; Gigli, G.; Sanvitto, D. Toward Cavity Quantum Electrodynamics with Hybrid Photon Gap-Plasmon States. *ACS Nano* **2016**, *10*, 11360–11368.
- (72) Bettles, R. J.; Gardiner, S. A.; Adams, C. S. Enhanced Optical Cross Section *via* Collective Coupling of Atomic Dipoles in a 2D Array. *Phys. Rev. Lett.* **2016**, *116*, 103602.
- (73) Shahmoon, E.; Wild, D. S.; Lukin, M. D.; Yelin, S. F. Cooperative Resonances in Light Scattering from Two-Dimensional Atomic Arrays. *Phys. Rev. Lett.* **2017**, *118*, 113601.
- (74) Perczel, J.; Borregaard, J.; Chang, D. E.; Pichler, H.; Yelin, S. F.; Zoller, P.; Lukin, M. D. Photonic Band Structure of Two-dimensional Atomic Lattices. *Phys. Rev. A: At., Mol., Opt. Phys.* **2017**, *96*, 063801.
- (75) Rodriguez, S. R. K.; Feist, J.; Verschuuren, M. A.; Garcia Vidal, F. J.; Gómez Rivas, J. Thermalization and Cooling of Plasmon-Exciton Polaritons: Towards Quantum Condensation. *Phys. Rev. Lett.* **2013**, 111, 166802.
- (76) Hakala, T. K.; Moilanen, A. J.; Väkeväinen, A. I.; Guo, R.; Martikainen, J.-P.; Daskalakis, K. S.; Rekola, H. T.; Julku, A.; Törmä, P. Bose–Einstein Condensation in a Plasmonic Lattice. *ar-Xiv:1706.01528v2* **2017**.
- (77) Kittel, C. Introduction to Solid State Physics; Wiley, 2005.
- (78) Kwadrin, A.; Koenderink, A. F. Diffractive Stacks of Metamaterial Lattices with a Complex Unit Cell: Self-Consistent Long-Range Bianisotropic Interactions in Experiment and Theory. *Phys. Rev. B: Condens. Matter Mater. Phys.* **2014**, *89*, 045120.
- (79) Lunnemann, P.; Koenderink, A. F. Dispersion of Guided Modes in Two-Dimensional Split Ring Lattices. *Phys. Rev. B: Condens. Matter Mater. Phys.* **2014**, *90*, 245416.
- (80) Humphrey, A. D.; Barnes, W. L. Plasmonic Surface Lattice Resonances on Arrays of Different Lattice Symmetry. *Phys. Rev. B: Condens. Matter Mater. Phys.* **2014**, *90*, 075404.
- (81) Wang, D.; Yang, A.; Hryn, A. J.; Schatz, G. C.; Odom, T. W. Superlattice Plasmons in Hierarchical Au Nanoparticle Arrays. ACS Photonics 2015, 2, 1789–1794.
- (82) Humphrey, A. D.; Barnes, W. L. Plasmonic Surface Lattice Resonances in Arrays of Metallic Nanoparticle Dimers. *J. Opt.* **2016**, *18*, 035005.

(83) Guo, R.; Hakala, T. K.; Törmä, P. Geometry Dependence of Surface Lattice Resonances in Plasmonic Nanoparticle Arrays. *Phys. Rev. B: Condens. Matter Mater. Phys.* **2017**, 95, 155423.

- (84) Humphrey, A. D.; Meinzer, N.; Starkey, T. A.; Barnes, W. L. Surface Lattice Resonances in Plasmonic Arrays of Asymmetric Disc Dimers. *ACS Photonics* **2016**, *3*, 634–639.
- (85) Schaafsma, M. C.; Bhattacharya, A.; Rivas, J. G. Diffraction Enhanced Transparency and Slow THz Light in Periodic Arrays of Detuned and Displaced Dipoles. *ACS Photonics* **2016**, *3*, 1596–1603.
- (86) Auguié, B.; Bendaña, X. M.; Barnes, W. L.; García de Abajo, F. J. Diffractive Arrays of Gold Nanoparticles Near an Interface: Critical Role of the Substrate. *Phys. Rev. B: Condens. Matter Mater. Phys.* **2010**, 82, 155447.
- (87) García de Abajo, F. J. Multiple Scattering of Radiation in Clusters of Dielectrics. *Phys. Rev. B: Condens. Matter Mater. Phys.* **1999**, 60, 6086–6102.
- (88) Kataja, M.; Hakala, T. K.; Julku, A.; Huttunen, M. J.; van Dijken, S.; Törmä, P. Surface Lattice Resonances and Magneto-Optical Response in Magnetic Nanoparticle Arrays. *Nat. Commun.* **2015**, *6*, 7072.
- (89) Vicencio, R. A.; Cantillano, C.; Morales-Inostroza, L.; Real, B.; Mejía-Cortés, C.; Weimann, S.; Szameit, A.; Molina, M. I. Observation of Localized States in Lieb Photonic Lattices. *Phys. Rev. Lett.* **2015**, 114. 245503.
- (90) Novotny, L.; Hecht, B. *Principles of Nano-Optics*; Cambridge University Press: New York, 2006.
- (91) Glasser, M. L.; Zucker, I. J. Theoretical Chemistry: Advances and Perspectives; New York, 1980; pp 67-139.
- (92) Kambe, K. Theory of Low-Energy Electron Diffraction 2. Cellular Method for Complex Monolayers and Multilayers. Z. Naturforsch. A 1968, 23, 1280–1294.
- (93) Palik, E. D. Handbook of Optical Constants of Solids; Academic Press: San Diego, 1985.
- (94) Johnson, P. B.; Christy, R. W. Optical Constants of the Noble Metals. *Phys. Rev. B* **1972**, *6*, 4370–4379.

Supporting information for: Hybridization of Lattice Resonances

Sebastian Baur, Stephen Sanders, and Alejandro Manjavacas*

Department of Physics and Astronomy, University of New Mexico, Albuquerque, New Mexico 87131, United States

E-mail: manjavacas@unm.edu

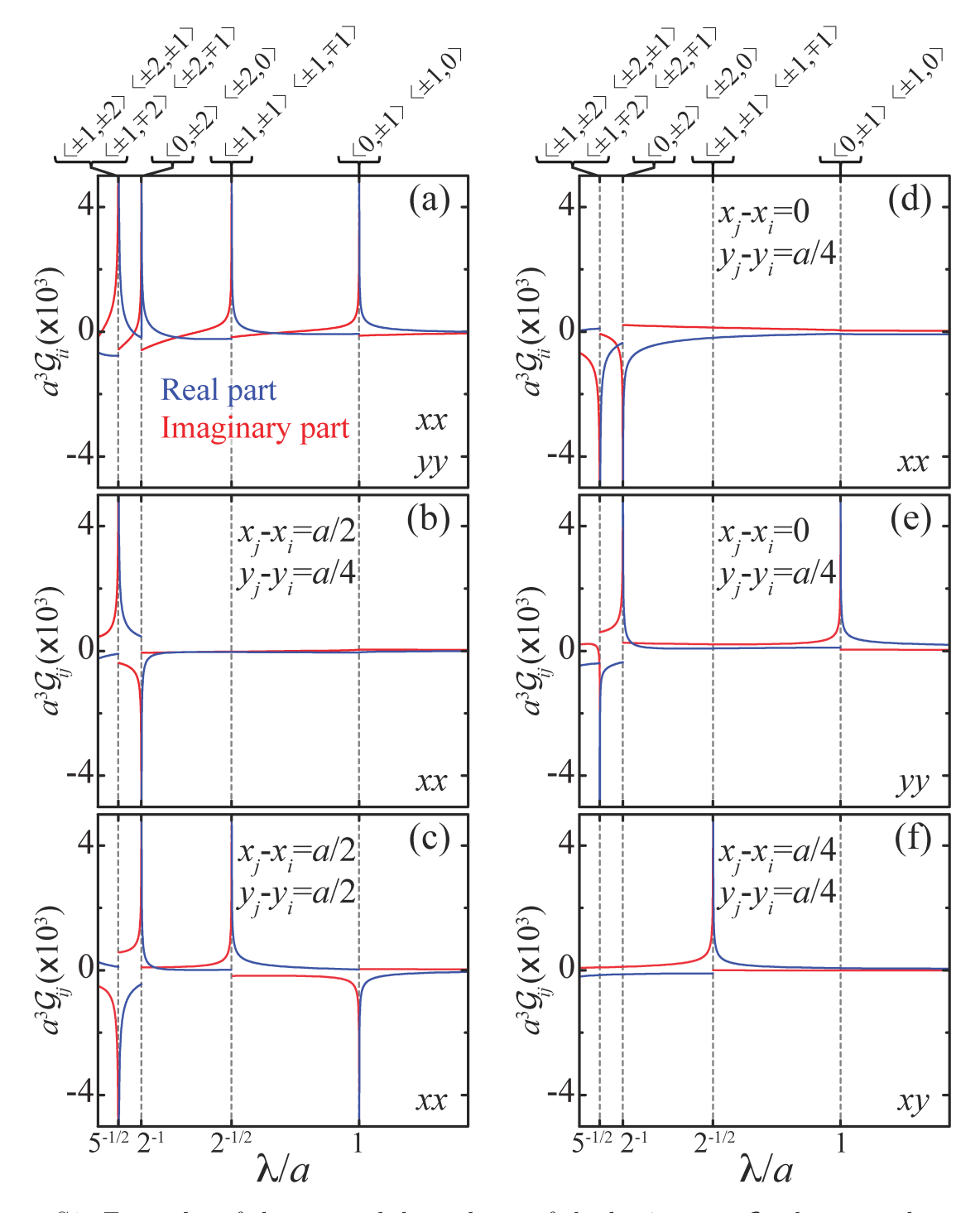


Figure S1: Examples of the spectral dependence of the lattice sum \mathcal{G}_{ij} that are relevant to some of the arrays studied in the main paper. In all cases, we consider a square array with periodicity a, and normal incidence. Blue and red curves are used to indicate the real and imaginary parts of the lattice sum, respectively. (a) xx component of \mathcal{G}_{ii} , which is identical to the yy component. (b) xx component of \mathcal{G}_{ij} for $x_j - x_i = a/2$, $y_j - y_i = a/4$. (c) xx component of \mathcal{G}_{ij} for $x_j - x_i = a/2$, $y_j - y_i = a/2$. (d) xx component of \mathcal{G}_{ij} for $x_j - x_i = 0$, $y_j - y_i = a/4$. (f) xy component of \mathcal{G}_{ij} for $x_j - x_i = a/4$.

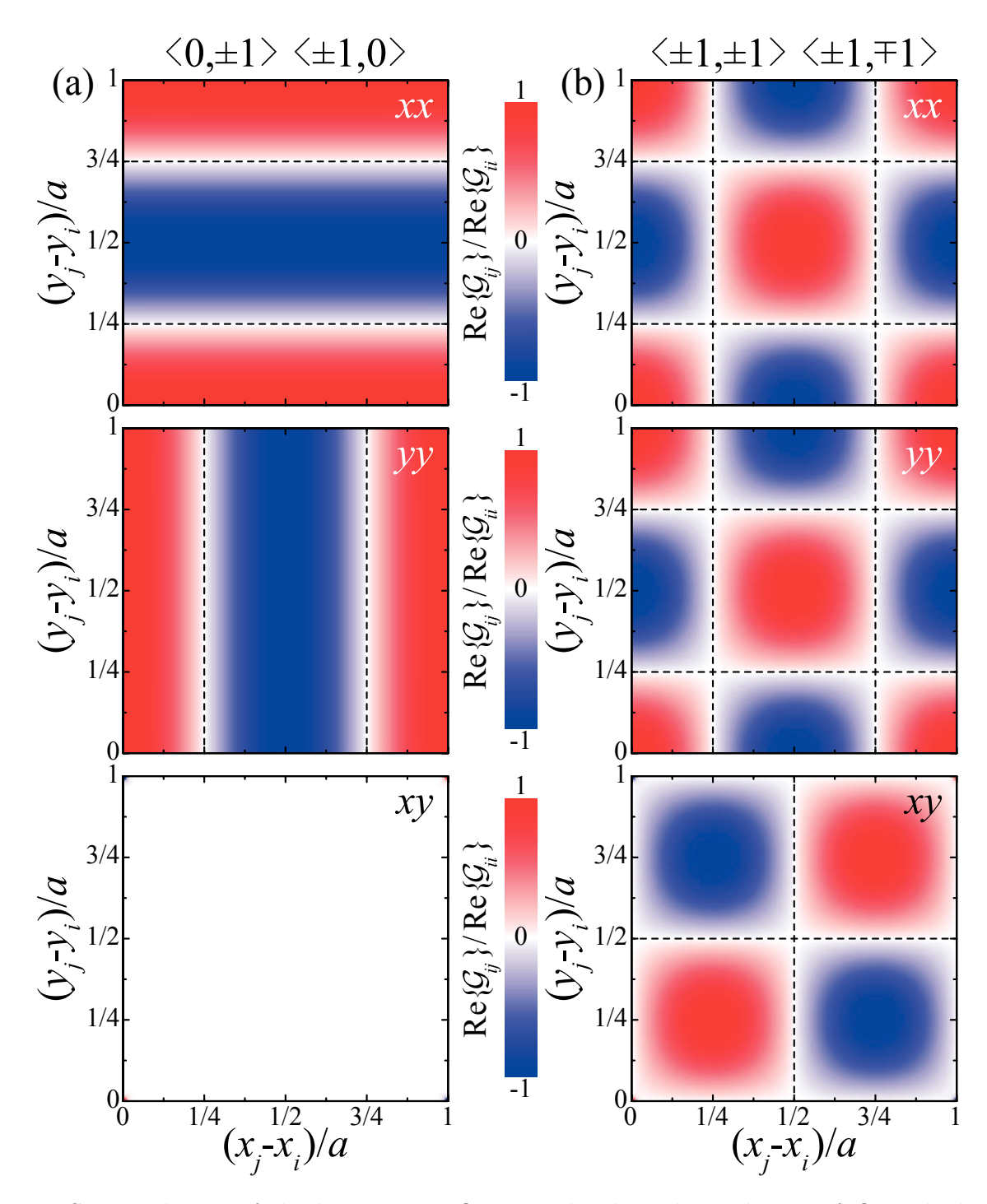


Figure S2: Real part of the lattice sum \mathcal{G}_{ij} normalized to the real part of \mathcal{G}_{ii} , calculated as a function of the position of particle j, measured with respect to particle i, for normal incidence. Panel (a) displays the results for the $\langle 0, \pm 1 \rangle$, $\langle \pm 1, 0 \rangle$ Rayleigh anomaly occurring at $\lambda = a$, while (b) displays the results for the $\langle \pm 1, \pm 1 \rangle$, $\langle \pm 1, \mp 1 \rangle$ Rayleigh anomaly, which appears in the spectrum at $\lambda = a/\sqrt{2}$. In both cases, the upper, middle, and lower plots correspond, respectively, to the xx, yy, and xy components of the lattice sum.

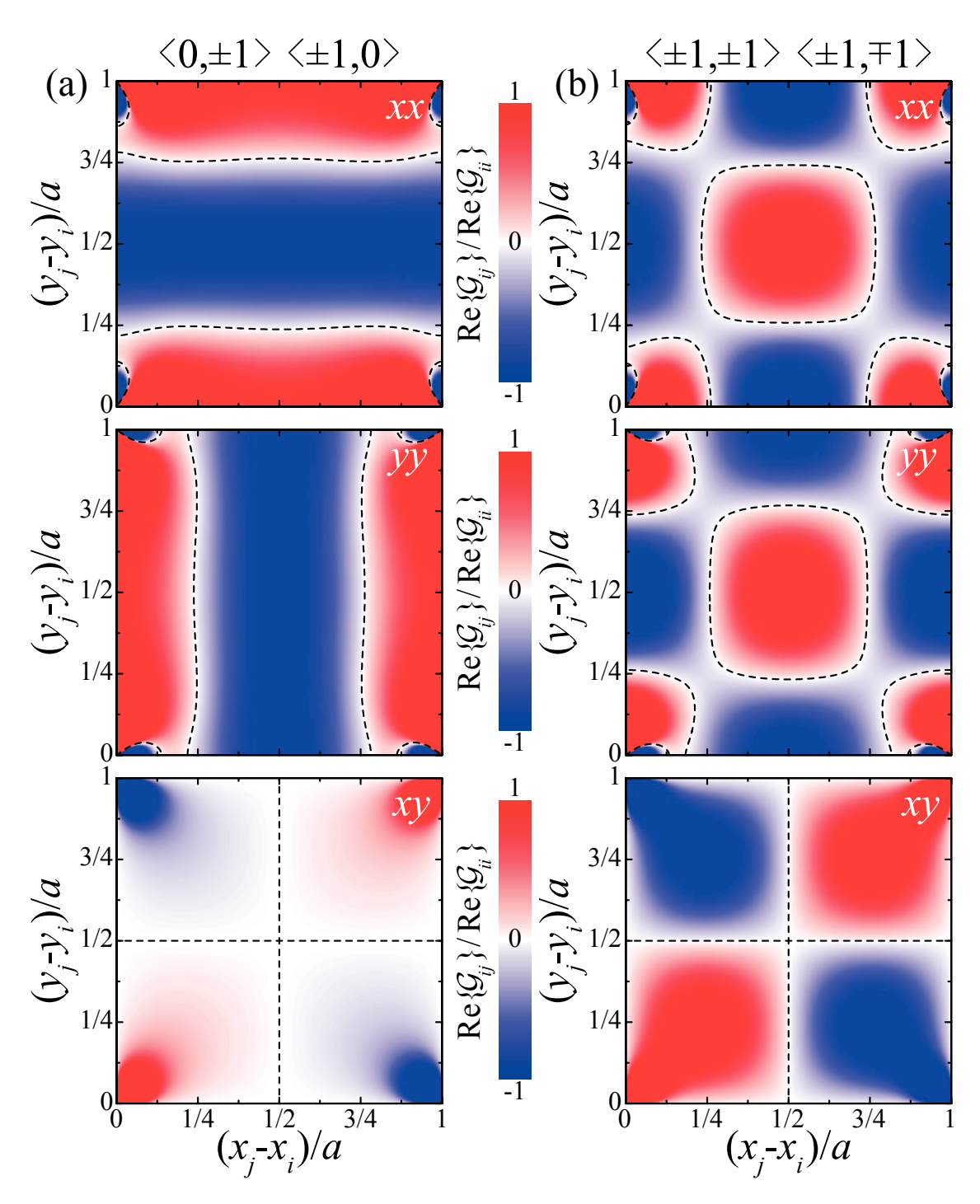


Figure S3: Same as Figure S2, but calculated at wavelengths $\lambda = 1.01a$ (a) and $\lambda = 1.01a/\sqrt{2}$ (b).

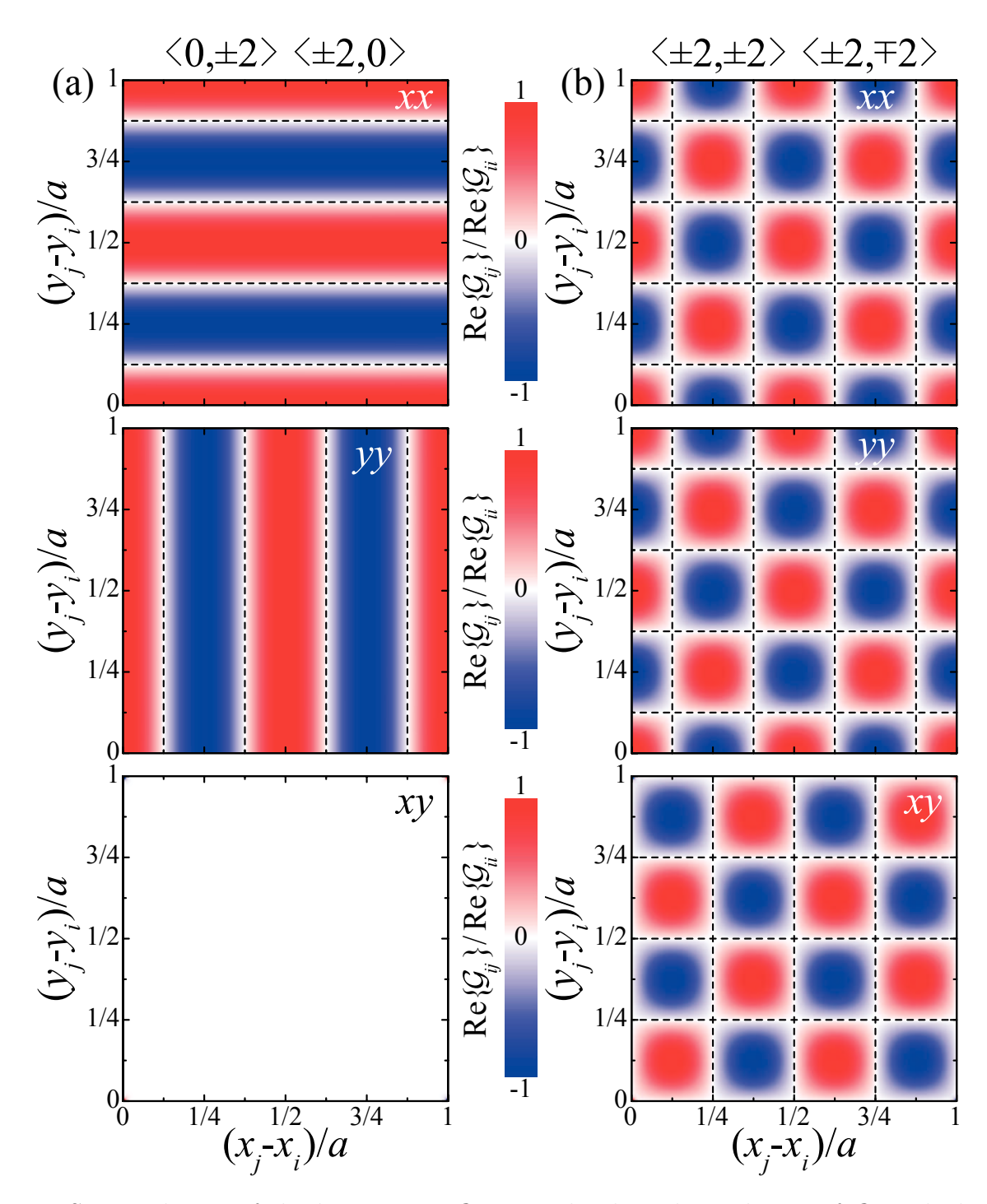


Figure S4: Real part of the lattice sum \mathcal{G}_{ij} normalized to the real part of \mathcal{G}_{ii} , calculated as a function of the position of particle j, measured with respect to particle i, for normal incidence. Panel (a) displays the results for the $\langle 0, \pm 2 \rangle$, $\langle \pm 2, 0 \rangle$ Rayleigh anomaly occurring at $\lambda = a/2$, while (b) displays the results for the $\langle \pm 2, \pm 2 \rangle$, $\langle \pm 2, \mp 2 \rangle$ Rayleigh anomaly, which appears in the spectrum at $\lambda = a/\sqrt{8}$. In both cases, the upper, middle, and lower plots correspond, respectively, to the xx, yy, and xy components of the lattice sum.

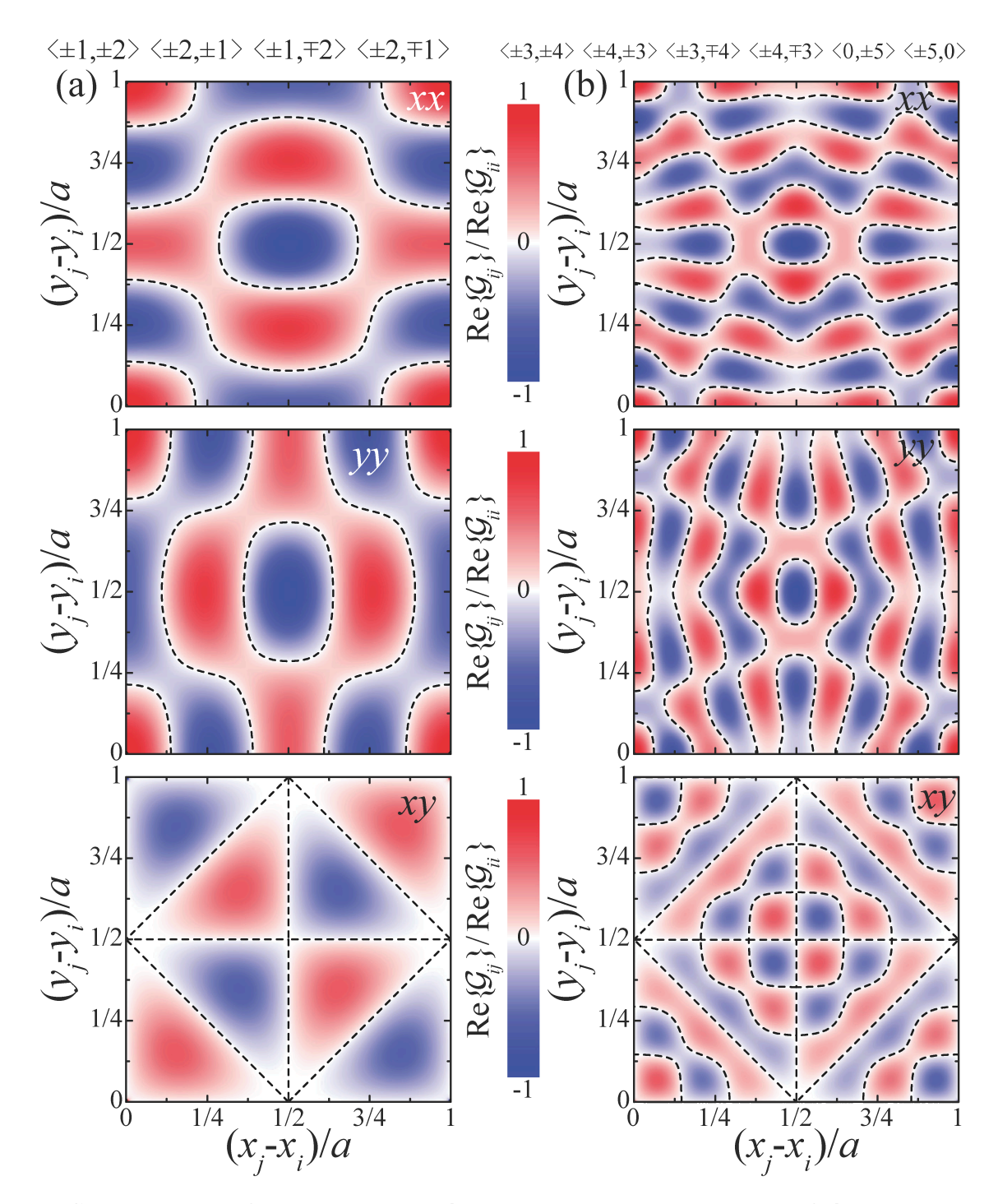


Figure S5: Real part of the lattice sum \mathcal{G}_{ij} normalized to the real part of \mathcal{G}_{ii} , calculated as a function of the position of particle j, measured with respect to particle i, for normal incidence. Panel (a) displays the results for the $\langle \pm 1, \pm 2 \rangle$, $\langle \pm 2, \pm 1 \rangle$, $\langle \pm 1, \mp 2 \rangle$, $\langle \pm 2, \mp 1 \rangle$ Rayleigh anomaly occurring at $\lambda = a/\sqrt{5}$, while (b) displays the results for the $\langle \pm 3, \pm 4 \rangle$, $\langle \pm 4, \pm 3 \rangle$, $\langle \pm 4, \mp 3 \rangle$, $\langle 0, \pm 5 \rangle$, $\langle \pm 5, 0 \rangle$ Rayleigh anomaly, which appears in the spectrum at $\lambda = a/5$. In both cases, the upper, middle, and lower plots correspond to the xx, yy, and xy components of the lattice sum, respectively.

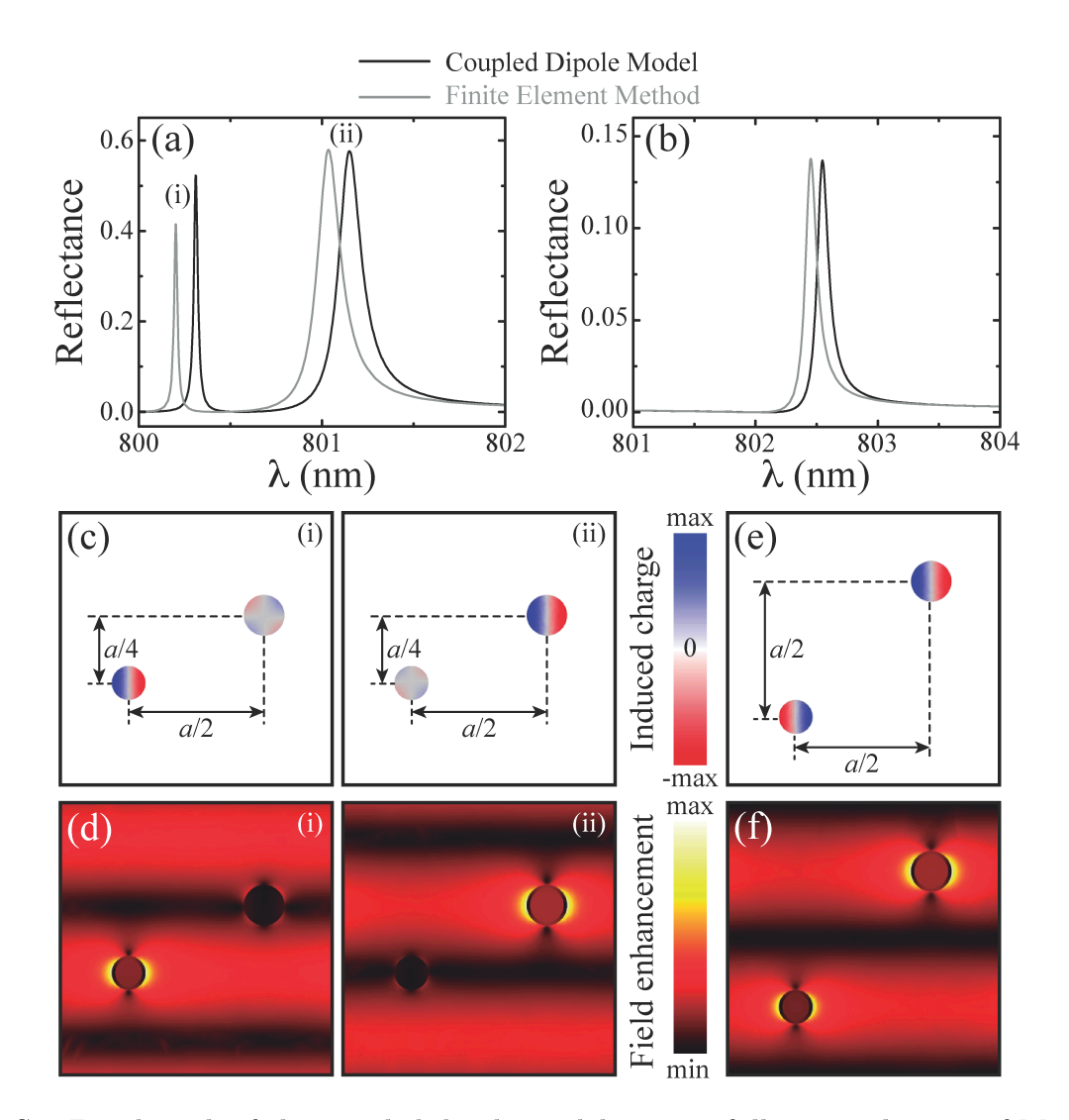


Figure S6: Benchmark of the coupled dipole model against full-wave solutions of Maxwell's equations obtained through a Finite Element Method (FEM) simulation, performed using the commercial software COMSOL Multiphysics. (a,b) Reflectance for the arrays investigated in Figures 3(a) and 3(e) of the main paper, both of which consist of a square lattice with periodicity $a = 800 \,\mathrm{nm}$ and a unit cell containing two silver nanoshells with silica cores and dimensions $R_{\rm i}=40\,{\rm nm},\ R_{\rm o}=50\,{\rm nm}$ for particle 1, and $R_{\rm i}=50\,{\rm nm},\ R_{\rm o}=60\,{\rm nm}$ for particle 2. The positions of the particles are $x_1 = 0$, $y_1 = 0$, and $x_2 = a/2$, $y_2 = a/4$ for the array of panel (a) and $x_1 = 0$, $y_1 = 0$, and $x_2 = a/2$, $y_2 = a/2$ for that of panel (b). The black curves represent the results obtained using the coupled dipole model, while the gray curves indicate the outcome of the FEM simulation. Both cases show an excellent agreement between the predictions of the coupled dipole method and the FEM simulations. The main difference is a shift of the peak position, which we attribute to the effect of the higher order modes not accounted for in the dipole approximation. (c,d) Charge density induced in the nanoshells (c), and field enhancement in the plane of the array (d), both calculated using the FEM approach for the two lattice resonances of the array of panel (a). (e,f) Same as panels (c) and (d) for the lattice resonance of the array of panel (b). These results confirm the predictions of Figure 3 of the main paper, and therefore support the validity of the coupled dipole model.

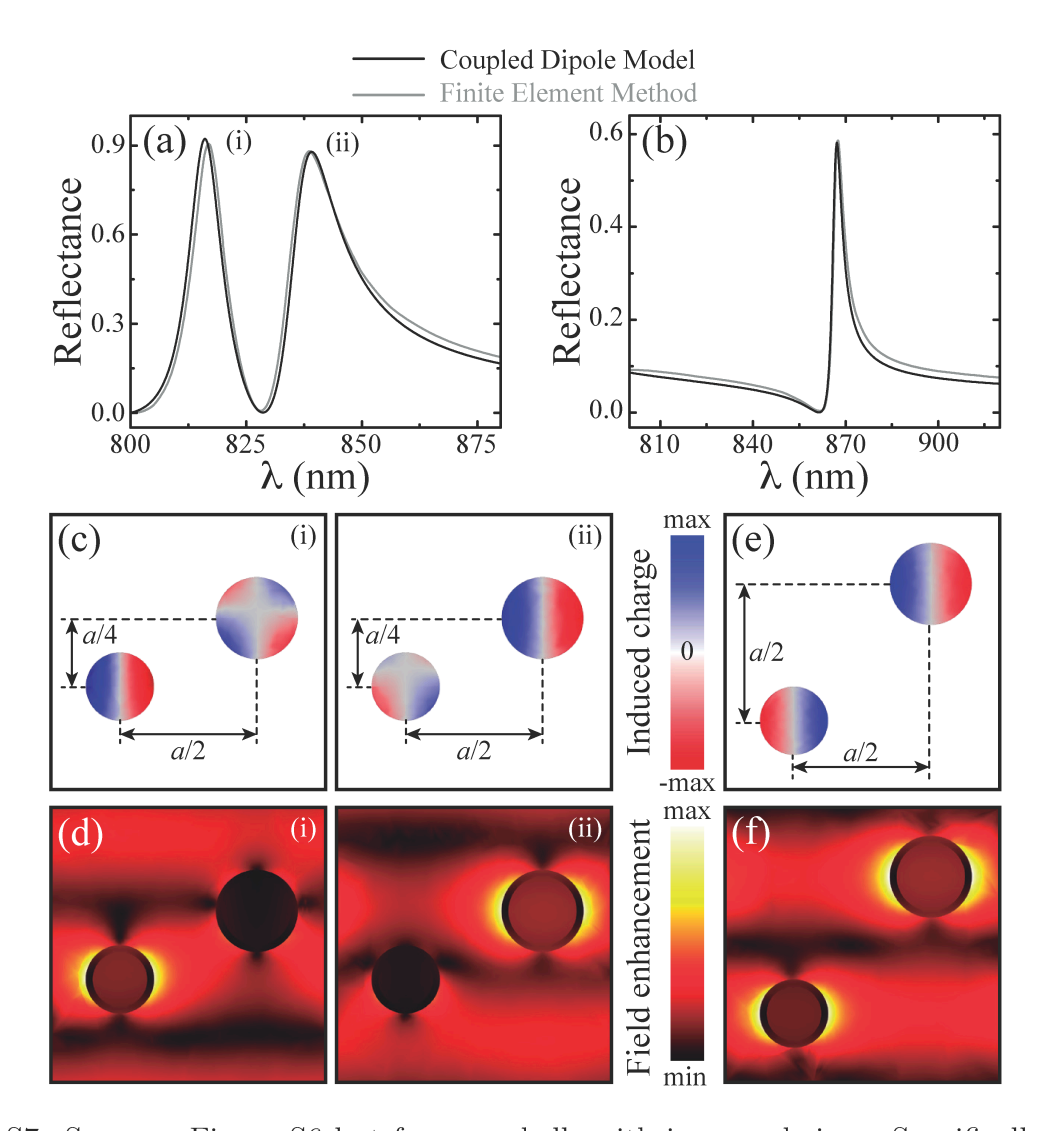


Figure S7: Same as Figure S6 but for nanoshells with increased sizes. Specifically, we use $R_{\rm i}=80\,{\rm nm},\,R_{\rm o}=100\,{\rm nm}$ for particle 1, and $R_{\rm i}=100\,{\rm nm},\,R_{\rm o}=120\,{\rm nm}$ for particle 2. The rest of the parameters are identical to those of Figure S6. The coupled dipole model results are in good agreement with the FEM simulations. As expected, the contribution of higher order modes is increased with respect to the systems of Figure S6, which leads to a larger shift between the coupled dipole model predictions and the FEM results, although this effect is partially masked by the increased linewidth of the resonances. The charge density and field enhancement maps also confirm the larger contribution of higher order modes.